



Contents lists available at ScienceDirect

# Physics of the Earth and Planetary Interiors

journal homepage: [www.elsevier.com/locate/pepi](http://www.elsevier.com/locate/pepi)

## Seismic signature of a hydrous mantle transition zone



Vincent Thio, Laura Cobden\*, Jeannot Trampert

Department of Earth Sciences, Utrecht University, Heidelberglaan 2, 3584CS Utrecht, The Netherlands

### ARTICLE INFO

#### Article history:

Received 2 April 2015

Received in revised form 2 November 2015

Accepted 18 November 2015

Available online 2 December 2015

#### Keywords:

Water

Transition zone

Seismology

Mineral physics

### ABSTRACT

Although water has a major influence on tectonic and other geodynamic processes, little is known about its quantity and distribution within the deep Earth. In the last few decades, laboratory experiments on nominally anhydrous minerals (NAMs) of the transition zone have shown that these minerals can contain significant amounts of water, up to 3.3 wt%. In this study, we investigate if it is possible to use seismic observations to distinguish between a hydrous and anhydrous transition zone. We perform an extensive literature search of mineral experimental data, to generate a compilation of the water storage capacities, elastic parameters and phase boundary data for potentially hydrous minerals in the transition zone, and use thermodynamic modelling to compute synthetic seismic profiles of density,  $V_p$  and  $V_s$  at transition zone temperatures and pressures. We find that large uncertainties on the mineral phase equilibria (ca. 2 GPa) and elastic properties produce a wide range of seismic profiles. In particular, there is a lack of data at temperatures corresponding to those along a 1300 °C adiabat or hotter, which may be expected at transition zone pressures. Comparing our hydrous transition zone models with equivalent profiles at anhydrous conditions, we see that the depths of the 410 and 660 discontinuities cannot at present be used to map the water content of the transition zone due to these uncertainties. Further, while average velocities and densities inside the transition zone clearly decrease with increasing water content, there is a near-perfect trade-off with increases in temperature. It is therefore difficult to distinguish thermal from water effects, and the conventional view of a slow and thick transition zone for water and slow and thin transition zone for high temperature should be regarded with caution. A better diagnostic for water may be given by the average velocity gradients of the transition zone, which increase with increasing water content (but decrease for increasing temperature). However the significance of this effect depends on the degree of water saturation and partitioning between the NAMs. Since seismology is better able to constrain the thickness of the transition zone than velocity gradients, our study indicates that the most useful input from future mineral physics experiments would be to better constrain the phase relations between hydrous olivine and its high-pressure polymorphs, especially at high temperatures. Additionally, the uncertainties on the mineral seismic properties could be reduced significantly if the experimentally-observable correlations between bulk and shear moduli and their corresponding pressure derivatives would be published.

© 2015 The Authors. Published by Elsevier B.V. This is an open access article under the CC BY-NC-ND license (<http://creativecommons.org/licenses/by-nc-nd/4.0/>).

### 1. Introduction

One of the prime characteristics that distinguishes the Earth from other terrestrial planets is the substantial amount of liquid water at its surface. Water plays a major role in the dynamics of our planet and is fundamental to the existence of organic life. Yet while the water cycle at the Earth's surface and atmosphere is widely studied and understood, little is known about the quantity, distribution or behaviour of water within the Earth. We know that water enters the mantle via subduction and is released via volcanism, but precisely how it cycles between those places is essentially

unknown. Water has a large influence on the physical properties of rocks. It reduces their strength, viscosity and melting point (Chen et al., 1998; Hirschmann, 2006), which in turn yields major consequences for large-scale processes such as volcanic activity, plate tectonics (Regenauer-Lieb et al., 2001) and possibly the generation of very deep (400–600 km) earthquakes (Richard et al., 2007). Therefore, in order to gain a better understanding of these processes, it is essential to constrain how much water is stored in the mantle and its distribution. This, in turn, requires us to determine the change in water solubility with respect to pressure, temperature and mineral type, and the effect which water has on the physical properties of mantle minerals.

The present-day total water volume found in oceans is about 0.025% of the total mass of the Earth, but this fraction may have

\* Corresponding author. Fax: +31 (0)30 253 2648.

E-mail address: [l.j.cobden@uu.nl](mailto:l.j.cobden@uu.nl) (L. Cobden).

been significantly higher during the early stages of the Earth's existence, ~4.5 billion years ago (Drake, 2005). This poses the question of what happened to the excess water; did it escape the atmosphere into space, or is a significant amount of water currently stored within the deep Earth? Field studies provide both supporting and opposing results for the latter: a recent study by Pearson et al. (2014) on a ringwoodite inclusion in a diamond found that the ringwoodite had a water content of 1.5 wt%, indicating that the mantle is (at least locally) subject to hydration. On the other hand, geochemical analysis of volcanic rocks by Dixon et al. (2002), together with numerical models of the deep mantle by Rupke et al. (2006), suggest that the deeper mantle is predominantly anhydrous.

Laboratory experiments in the last two decades on the water storage capacity of major mantle minerals previously thought to be anhydrous, the so called 'nominally anhydrous minerals' (NAMs), have shown that they actually have the capacity to absorb small weight percentages of water, in the form of structurally bound (OH<sup>-</sup>) ions. When integrated over the whole volume of the Earth, the mantle could therefore, theoretically, contain significant amounts of water, up to several times the total water volume currently found in the oceans (Smyth and Jacobsen, 2006). Two minerals in particular, wadsleyite and ringwoodite, have been found to have a significant water storage capacity of up to several weight percent (Ohtani et al., 2000; Chen et al., 2002). These high-pressure polymorphs of olivine make up about 60% of the transition zone, a region in the mantle between approximately 410 and 660 km depth which is characterised by high velocity gradients. The transition zone is bounded on both sides by sharp increases in velocity, the so-called '410' and '660' discontinuities, which are thought to arise from the phase transition of olivine to wadsleyite, and the decomposition of ringwoodite into perovskite and magnesiowüstite, respectively. Since wadsleyite and ringwoodite have much greater water storage capacity than the overlying olivine or underlying perovskite, the transition zone could be a major water reservoir, where water entering the mantle by subduction becomes trapped between the relatively dry minerals above and below the transition zone (the so-called 'transition-zone water filter' of Bercovici and Karato (2003)).

Constraints on the physical properties of the mantle are predominantly obtained from seismic observations. Three main structural aspects of the transition zone are expected to be influenced by water and might be seen in seismic data: These are (1) the velocity profile of the transition zone, (2) the position (i.e. depth) of the '410' and '660' discontinuities and (3) the impedance contrast at the '410' and '660' discontinuities. Recent experiments on the elastic properties of NAMs indicate that both  $P$  and  $S$  wave speed decrease with increasing water content (e.g. Jacobsen and Smyth, 2006). It is thus possible that the average velocity in the hydrous transition zone will be lower than at anhydrous conditions, and that the impedance contrast at the '410' and '660' discontinuities will decrease and increase, respectively, assuming that the minerals above and below the transition zone contain significantly less water. Studies on the phase transitions between olivine and its high-pressure polymorphs indicate that the olivine-wadsleyite transition occurs at slightly lower pressures (Smyth and Frost, 2002) under hydrous conditions, and the post-spinel composition at slightly higher pressures (e.g. Litasov et al., 2005; Ghosh et al., 2013). However, this is a relatively young and active area of research, and experimental data are only available at limited ( $P$ ,  $T$ ) conditions. In particular, experimental data are often obtained at lower pressures than the transition zone, and whether hydrous NAMs remain slower than anhydrous NAMs at transition zone pressures depends heavily on the pressure derivatives of their elastic moduli. It is thus unclear how uncertainties in the experimental data translate into uncertainties in seismic properties,

and whether the existing data are sufficiently comprehensive to allow quantitative and robust interpretation of seismic observations in terms of water content.

At the same time, mapping the water content inside the transition zone using seismology is non-trivial for two main reasons. Firstly, the seismic structure is also modified by changes in temperature and major element chemistry (e.g. Fe content), meaning that there may be a non-unique physical interpretation for a given seismic structure. Karato (2011) has argued that the influence of water on seismic velocities is so small that variations in water content may be masked by changes in temperature or chemistry, to which seismic velocities are more sensitive. Secondly, the seismic data themselves each have uncertainties and limited resolving power, and in light of this it is unclear if the differences in seismic structure between anhydrous and hydrous transition zone regions are significant enough to be resolved by seismology.

In this study we explore how the ranges and limitations of the currently-available mineral experimental data for NAMs are mapped into seismic structure. We first make a compilation of experimental observations of hydrous NAMs, and then use thermodynamic modelling to predict corresponding wave speed and density profiles through the mantle transition zone. We do this in order to quantify the effect of water on the density and wave speeds at the '410', '660' and within the transition zone, relative to uncertainties in the mineral experimental data and changes in temperature and composition. We compare our findings to real seismic observations to investigate whether, at present, seismic observations have the capacity to identify water inside the mantle transition zone. Our results can be used as a guide for future seismic and mineralogical investigations, so that they may be optimised towards mapping water inside the transition zone.

## 2. Methodology

In order to calculate the seismic properties of a hydrous transition zone, we need to know the elastic properties of the constituent minerals at every temperature and pressure within the transition zone. To this end, we use the equation of state (EoS) of Stixrude and Lithgow-Bertelloni (2005) to extrapolate mineral elastic properties from ambient conditions to high  $P$  and  $T$ . This EoS is essentially a third order Birch–Murnaghan finite strain extrapolation for pressure with a Mie–Grüneisen correction for temperature. The computer program *Perple\_X* (Connolly, 1990, 2005) is used to solve the EoS. For a given bulk composition, set of mineral elastic properties and pressure–temperature range, *Perple\_X* applies the EoS to derive the elastic properties per mineral at each point within a 2D-grid of pressure and temperature points. Simultaneously, *Perple\_X* computes the stable mineral assemblage at each  $P$ – $T$  point via a free energy minimisation. The overall physical properties of the bulk mineral assemblage are computed from a weighted average of the constituent minerals: in our case the desired properties are the Voigt–Reuss–Hill (VRH) average for  $P$  and  $S$  wave speed, and the Voigt average for density. *Perple\_X* then outputs the desired properties along a given  $P$ – $T$  path by interpolation of the local elastic properties at the nearest grid points.

The thermoelastic dataset of Stixrude and Lithgow-Bertelloni (2011) was used as the primary input for all calculations. This dataset is composed of 47 minerals and mineral end-members, each described in terms of 10 thermodynamic parameters: the Helmholtz free energy ( $F_0$ ), volume ( $V_0$ ), isothermal bulk modulus ( $K_{T0}$ ), shear modulus ( $G_0$ ), their pressure derivatives ( $K'_0$ ,  $G'_0$ ), Debye temperature ( $\theta_0$ ), Grüneisen parameter ( $\gamma_0$ ), and two parameters related to the temperature derivatives of the bulk and shear moduli ( $q$ ,  $\eta_{S0}$ ), where the subscript '0' represents ambient conditions. These parameters have been obtained by a global inversion of experimental data allowing mineral elastic properties and phase

equilibria to be derived within a self-consistent framework simultaneously.

The chemical compositions in our models are defined in terms of up to five oxides: CaO, FeO, MgO, Al<sub>2</sub>O<sub>3</sub> and SiO<sub>2</sub> (CFMAS). These oxides comprise about 98% of the mantle volume. The target composition of our modelling is pyrolite, since this is often assumed to be the average mantle composition (e.g. Anderson, 2007). In this study, pyrolite is composed of the following molar percentages of oxides: 3.25% CaO, 6.24% FeO, 49.13% MgO, 2.77% Al<sub>2</sub>O<sub>3</sub> and 38.61% SiO<sub>2</sub> (from Sun (1982)) (the composition expressed as weight% equivalent is: 3.5% CaO, 8.6% FeO, 38.0% MgO, 5.4% Al<sub>2</sub>O<sub>3</sub>, and 44.5% SiO<sub>2</sub>). However, before inferring the seismic properties of a hydrous pyrolite, it was first instructive to study two simpler compositions: ‘Fo100’ (where ‘Fo’ stands for forsterite) for studying the elastic properties of pure Mg<sub>2</sub>SiO<sub>4</sub>, composed of 66.6% MgO, 33.3% SiO<sub>2</sub> (percentage in mol), and a mixed Fe–Mg composition, composed of either 60% MgO, 6.6% FeO, 33.3% SiO<sub>2</sub> (Fo90), or 53.3% MgO, 13.3% FeO, 33.3% SiO<sub>2</sub> (Fo80).

To compute the seismic properties of hydrous models using *Perple\_X*, we do not add (OH) to the bulk composition as input to *Perple\_X* but rather for a given CFMAS composition, we incorporate the effect of water by adjusting the 10 input thermodynamic parameters of the anhydrous NAMs to those of their hydrated counterparts. We performed an extensive literature compilation in order to define these “hydrous” parameters, as a function of water content, described in Section 3.3. We also searched the literature to determine the range of plausible water contents per NAM (Section 3.1) and how water is partitioned between the NAMs (Section 3.2).

The experimental data for the elastic properties and phase relations of the NAMs have non-negligible uncertainties, and one of our main goals is to understand the seismic manifestation of these uncertainties. We therefore computed 10,000 models per CFMAS–water composition. For each model the NAM elastic properties and phase boundaries were chosen at random within pre-defined uncertainty ranges, in a Monte-Carlo procedure. These uncertainty ranges were defined from our own literature search (Section 3.3). For comparison, we also ran simulations of 10,000 models containing no water, in which the elastic properties of the (anhydrous) NAMs were varied within the uncertainties published by Stixrude and Lithgow-Bertelloni (2011).

We assume an adiabatic  $P$ – $T$  path through the mantle, implying a constant entropy along the path. An adiabatic thermal structure arises if the mantle is vigorously convecting. We base our main models on an adiabat with a potential temperature of 1573 K (following Cobden et al. (2008)), but hotter ( $T_{\text{pot}} = 1773$  K) and colder ( $T_{\text{pot}} = 1373$  K) adiabats are also considered.

There are several features of the thermodynamic modelling which should be taken into account: firstly, the NAMs whose properties will be modified are solid solutions of Mg and Fe, and as input, *Perple\_X* requires elastic parameters of the Fe and Mg end-members only. In general, data for pure Fe end-members of hydrous NAMs are sparse, especially at high temperatures. Secondly *Perple\_X* assumes a constant bulk composition with pressure and temperature. Thirdly, we do not correct the seismic velocities for intrinsic anelasticity, since it is unknown how to quantify the effect of water on mineral anelasticity (e.g. Karato, 2011).

Our steps for computing velocity and density profiles can be summarised as follows:

1. The bulk anhydrous chemical composition is defined, described in terms of the molar percentage of up to 5 main oxide end-members (CaO, FeO, MgO, Al<sub>2</sub>O<sub>3</sub> and SiO<sub>2</sub>).
2. The water content of wadsleyite is determined. Wadsleyite has the highest storage capacity of the NAMs (Section 3.1), and water contents of olivine and ringwoodite are derived relative

to this, using partition coefficients (usually 1:6:3, Section 3.2). All other mantle minerals are assumed to be anhydrous (see Section 3.1).

3. Mineral elastic parameters for the chosen water contents are defined at ambient conditions. For anhydrous minerals we use the thermoelastic dataset of Stixrude and Lithgow-Bertelloni (2011) and for hydrous minerals we define our own parameters with uncertainty bounds based on the available literature (Section 3.3).
4. These elastic parameters are extrapolated from ambient conditions to mantle pressures and temperatures for each of the minerals by *Perple\_X*, using the equation of state of Stixrude and Lithgow-Bertelloni (2005). Simultaneously, phase boundaries and mineral compositions at each  $P$ – $T$  point on the 2D grid are calculated intrinsically within *Perple\_X* by combining the elastic parameters with solid solution data of Stixrude and Lithgow-Bertelloni (2011).
5. For a given 1-D  $P$ – $T$  profile (typically a 1573 K adiabat) along which we wish to compute seismic properties, we extract the bulk modulus  $K$ , shear modulus  $G$  and density  $\rho$  of each mineral along the profile. The densities of the NAMs are updated to include the effect of water in the crystal structure, which cannot be computed intrinsically (Appendix A2).
6. The  $K$ ,  $G$  and updated  $\rho$  values are then used to compute the average density and  $P$  and  $S$  velocities of the bulk mineral assemblage, using a Voigt (for density) or Voigt–Reuss–Hill (for  $K$  and  $G$ ) averaging scheme.

Steps 1–6 were repeated 10,000 times for each CFMAS–water composition and thermal structure of interest.

### 3. Data compilation and uncertainties for the transition zone NAMs

#### 3.1. Water storage capacity

Water can have a significant effect on the elastic properties of a mineral, and therefore on the velocity profile of the mantle. However, the water storage capacity differs per mineral, with some minerals having very low storage capacities (e.g. stishovite, garnet. Bolfan-Casanova et al. (2000) and Aubaud et al. (2008)) whereas others have capacities up to 3.8 wt% (Fe-free wadsleyite, Chen et al. (2002)). Therefore, it is not realistic to assume a single water content for the whole upper mantle. Instead, we undertook a literature study of the water storage capacities of each NAM and determined the water content separately per mineral.

In this study we will focus on the water contents of olivine, wadsleyite and ringwoodite, and assume all other NAMs to be anhydrous. Most other minerals are volumetrically small within the transition zone, so even if they could store large amounts of water it would most likely have little effect on the seismic profile. Garnet does occupy a large volume fraction (ca. 40%), but its low water storage capacity (less than 0.1 wt%, Aubaud et al. (2008)) is assumed to have a small seismic effect. We further assume that perovskite is anhydrous, since data on the elastic properties of hydrous perovskite are not yet available, and most experiments indicate that its water storage capacity is extremely low, such that significant changes in its seismic properties are unlikely. Reported values of water uptake by perovskite are 0.01 wt% (Litasov and Ohtani, 2003), 0.05 wt% (Higo et al., 2006), <~0.1 wt% (Inoue et al., 2010a), and a few ppm (Bolfan-Casanova et al., 2003). While some older lab experiments (e.g. Murakami et al. (2002)) and recent first principles calculations (Hernández et al., 2013) have suggested water uptake can reach 0.1–0.2 wt%, the most recent lab experiments at lower mantle conditions suggest that perovskite is essentially dry (Panero et al., 2015), and where water

is added to perovskite samples, it likely sits on grain boundaries or in fluid inclusions rather than being incorporated into the crystal structure (e.g. Schmandt et al. (2014)). The other major mineral of the lower mantle, periclase, is also unlikely to host significant water (e.g. Bolfan-Casanova et al. (2002) and Hernández et al. (2013)).

### 3.1.1. Olivine

Storage capacities of up to 0.9 wt% have been found for olivine (Smyth and Jacobsen, 2006), but are generally lower depending on pressure, temperature and Fe-content (Zhao et al., 2004; Litasov et al., 2007; Deon et al., 2011; Ferot and Bolfan-Casanova, 2012). Kohlstedt et al. (1996) found much lower values, up to 0.15 wt% in San Carlos olivine ( $Mg_{0.9}Fe_{0.1}SiO_4$ ), but Mosenfelder et al. (2006) used a different calibration method and obtained 0.64 wt% water for Fe-bearing olivine. This was also found by Chen et al. (2002), who investigated the storage capacity of San Carlos olivine between 12.6 and 14.6 GPa and at a temperature of 1473 K. Deon et al. (2011) tested the storage capacity at varying pressure and found a positive correlation. They also found that Fe increases the storage capacity at transition zone conditions

(12.6–14.6 GPa), which agrees with low-pressure experiments done by Zhao et al. (2004), but not with Litasov et al. (2007), who observed marginally lower maximum concentration in Fe-bearing olivine (0.6–0.7 wt% at 1673 K), compared to Fo100 (0.9 wt%) at the same conditions.

The effect of temperature on water storage capacity is unclear. Zhao et al. (2004) report a clear increase in solubility with increasing temperature (an increase from 1273 K to 1573 K results in more than twice the capacity), while other papers (Smyth et al., 2006; Litasov et al., 2007) conclude the opposite.

Available data for hydrous olivine is plotted in Fig. 1 (top). The data clearly show an increase in water content with pressure and decrease with temperature. The difference between Fe-bearing (squares) and Fe-free (circles) olivine is not directly clear from our compiled data set, which shows contradicting information at low temperature and high pressure. The red star indicates a representative  $P$ - $T$  point on the 1573 K adiabat above the transition zone (around 330 km depth; see also Fig. 4, bottom right) that we used to determine the average water content of saturated olivine. This average value of 0.25 wt% was used to estimate the partition coefficient between NAMs.

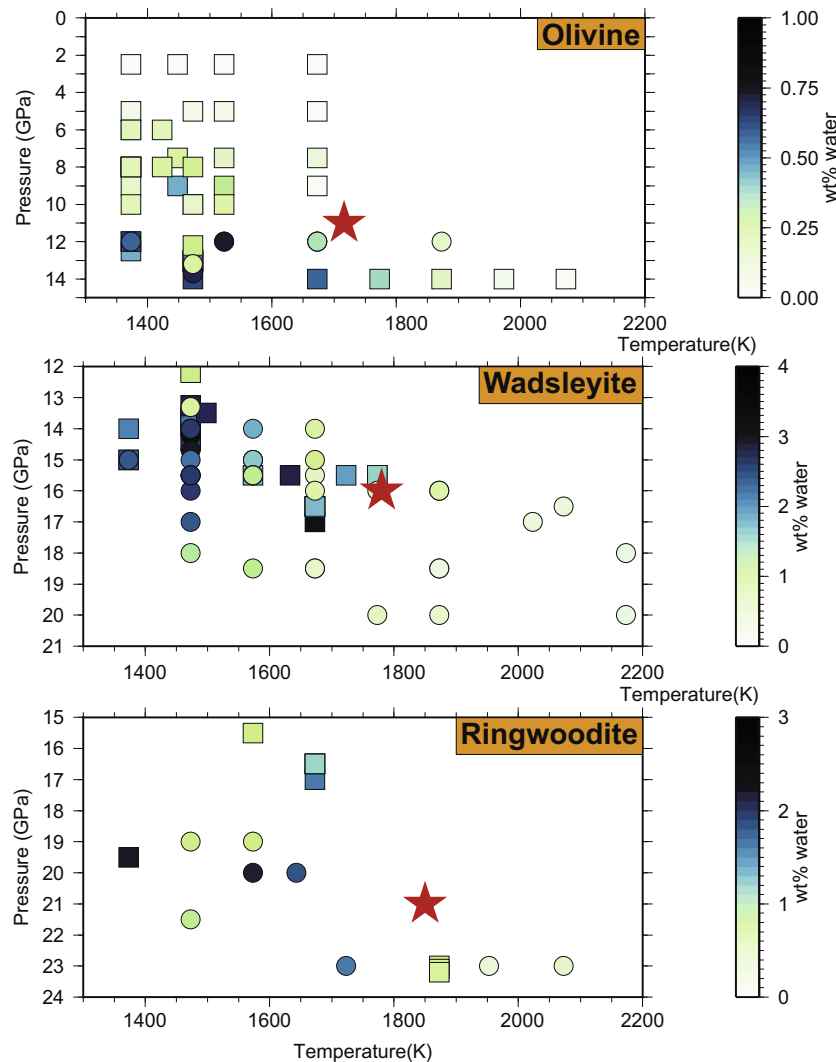


**Fig. 1.** Water storage capacity per NAM as a function of temperature and pressure. Circles indicate Fe-free samples, squares indicate Fe-bearing samples. The red stars indicate median pressure and temperature per phase in its field of stability along the 1573 K adiabat in pyrolite, below 300 km depth. These  $P$ - $T$  points correspond to those indicated in Fig. 4 (bottom, right). Data are taken from Bolfan-Casanova et al. (2000), Chen et al. (2002), Demouchy et al. (2005), Deon et al. (2011), Ferot and Bolfan-Casanova (2012), Inoue et al. (2010b,a), Kawamoto et al. (1996), Kohlstedt et al. (1996), Litasov and Ohtani (2003), Litasov et al. (2007, 2011), Mosenfelder et al. (2006), Ohtani et al. (2000), Smyth and Jacobsen (2006). (For interpretation of the references to colour in this figure legend, the reader is referred to the web version of this article.)

### 3.1.2. Wadsleyite

Wadsleyite has the highest storage capacity of the NAMs, first inferred theoretically by Smyth (1987) and later shown experimentally by Inoue et al. (1995). Since then, numerous studies have measured the storage capacity of wadsleyite as a function of pressure, temperature and Fe-content (e.g. Litasov and Ohtani, 2003; Jacobsen et al., 2005; Inoue et al., 2010a). In Fe-free wadsleyite, storage capacities of up to 3.5–3.8 wt% have been found by Chen et al. (2002), who performed their experiments within a pressure range of 14.2–14.7 GPa and at a constant temperature of 1473 K. For Fe-bearing wadsleyite, they found slightly lower but still significant storage capacities of 1.9–3.4 wt% at the same conditions, which agrees with values found by Kohlstedt et al. (1996) and Kawamoto et al. (1996), who report 2.4 wt% at 1373 K and 14–15 GPa, and 1.52 wt% at 1773 K and 15.5 GPa, respectively. Bolfan-Casanova et al. (2000), on the other hand, report much lower solubilities in wadsleyite of only 0.22 wt% at 15 GPa and 1573 K.

Demouchy et al. (2005) studied the water content of saturated Fe-free wadsleyite over a pressure range of 13–18 GPa ( $T = 1473$  K) and temperature range 1173–1673 K ( $P = 15$  GPa), to investigate the influence of  $T$  and  $P$  on water absorption. They found that pressure does not have a major influence, but that increasing temperature decreases the storage capacity significantly. This was also found by Litasov et al. (2011), whose study extended to higher pressures and temperatures (with Fe-free composition).

Fig. 1 (middle) shows available data for water content of wadsleyite as a function of temperature and pressure. At 1473 K, the storage capacities of Fe-free (circles) and Fe-bearing (squares) wadsleyite are roughly the same, but a significant decrease occurs for Fe-free wadsleyite at higher temperatures, whereas only a slight decrease occurs in the Fe-bearing compositions. The red star, representing the median pressure and temperature of a 1573 K adiabat in the wadsleyite stability field, corresponds to a value of  $\sim 1.5$  wt% water.

### 3.1.3. Ringwoodite

Ringwoodite has the second highest water storage capacity after wadsleyite, reportedly up to 2.7 wt% (Kohlstedt et al., 1996). A negative correlation with temperature was found for both Fe-free (Ohtani et al., 2000) and Fe-bearing ringwoodite (combining the data of Kohlstedt et al. (1996) and Inoue et al. (2010a,b)), but the pressure dependence is unclear. Recently, Pearson et al. (2014) studied the water content of a ringwoodite inclusion in a diamond, thought to have originated in the transition zone. They found a water content of 1.5 wt%, which suggests that ringwoodite is indeed (locally) hydrous within the transition zone. A compilation of the data from these and other papers is shown in Fig. 1. The average pressure and temperature along the 1573 adiabat for pyrolite within the ringwoodite stability field, indicated by the red star, yields an average value of  $\sim 0.8$  wt% water.

### 3.2. Partition coefficients

The water partition coefficient between two minerals specifies how a given amount of water is divided between the minerals at the phase boundary. Previous measurements of the partition coefficient of wadsleyite/olivine  $D_{\text{wad}/\text{oli}}$  vary between 1.8 and 6.0 (Chen et al., 2002; Demouchy et al., 2005; Smyth and Jacobsen, 2006; Litasov and Ohtani, 2008; Inoue et al., 2010b; Litasov et al., 2011) and of wadsleyite/ringwoodite  $D_{\text{wad}/\text{ring}}$  between 1.63 and 2.5 (Inoue et al., 2010a; Deon et al., 2011), indicating that the water partitioning is poorly constrained. In this study we derive water partition coefficients from the compiled dataset of the storage capacity per NAM (Fig. 1; Section 2.2). Since we assume constant water content per NAM, we compute the water partition coefficients from the

maximum expected water contents at mantle conditions. These are  $\sim 0.25$  wt%,  $\sim 1.5$  wt% and  $\sim 0.8$  wt% for olivine, wadsleyite and ringwoodite, respectively, resulting in partition coefficients  $D_{\text{wad}/\text{oli}} = 6.0$  and  $D_{\text{wad}/\text{ring}} = 2.0$ , or  $D_{\text{oli:wad:ring}} = 1:6:3$ . These values are compatible with the results of Inoue et al. (2010a), who studied the water partitioning of a pure-Mg composition and found 5:30:15:1 for olivine:wadsleyite:ringwoodite:perovskite.

### 3.3. Elastic parameters

We sought to assemble a new dataset of the 10 elastic parameters required by the equation of state of Stixrude and Lithgow-Bertelloni (2005) for hydrous olivine, wadsleyite and ringwoodite, including uncertainties, and for both the Mg and Fe end-members. We obtained these new parameter values primarily from experimental data, but if limited data were available, we constrained the parameters either theoretically from other mineral parameters, iteratively from indirect experimental data (e.g. changing  $F_0$  and  $\theta_0$  iteratively until the computed phase boundary matches the phase boundary from experiments), or by using systematic relationships from anhydrous minerals.

#### 3.3.1. Volume, bulk modulus and shear modulus ( $V_0$ , $K_{T0}$ , $G_0$ , $K'_0$ , $G'_0$ )

Sufficient experimental data were available to determine five of the required elastic parameters of  $\text{Mg}_2\text{SiO}_4$  at hydrous conditions directly:  $V_0$ ,  $K_{T0}$ ,  $G_0$ ,  $K'_0$ ,  $G'_0$ . Uncertainty bounds on these parameters were taken conservatively such that most experimental data points, including their experimental error bars, are lying within these bounds (see Fig. 2). Data falling outside these bounds either show large uncertainties or do not follow the general trend (e.g. the volume measurement for wadsleyite at 2.6 wt% water). Much of the uncertainty in these data stems from determination of the water content; typically this has been inferred from unpolarised IR values, and we can expect tighter constraints to be provided in the near-future from more sensitive methods such as proton-proton scattering and SIMS (S. Jacobsen, pers. comm.). In general the bulk and shear moduli of  $\text{Mg}_2\text{SiO}_4$  polymorphs decrease with increasing water content, but their pressure derivatives may increase (Fig. 2). Hypothetically this could lead to a “velocity crossover” where the hydrous minerals are slower than the anhydrous ones at low pressure but become faster at greater depths, as suggested by Mao et al. (2010). However it is difficult to predict the net effect on seismic velocities on the basis of  $K$ ,  $G$  and their pressure derivatives alone, since the temperature dependence also plays a role.

No data was found for the elastic properties of pure Fe mineral end-members ( $\text{Fe}_2\text{SiO}_4$ ), but limited data was available for (Mg, Fe)-mixtures (typically 10–20% Fe). To determine the elastic properties for the Fe end-members, we used the difference between the Fe and Mg end-member values at anhydrous conditions (from Stixrude and Lithgow-Bertelloni (2011)). The elastic properties of  $\text{Fe}_2\text{SiO}_4$  as a function of water content could then be determined by extrapolating properties of hydrous  $\text{Mg}_2\text{SiO}_4$  along the same trend as the difference between the anhydrous  $\text{Mg}_2\text{SiO}_4$  and  $\text{Fe}_2\text{SiO}_4$  values. In other words,

$$M_{\text{Fe}_2\text{SiO}_4, \text{hydrous}} = M_{\text{Mg}_2\text{SiO}_4, \text{hydrous}} + (M_{\text{Fe}_2\text{SiO}_4, \text{anhydrous}} - M_{\text{Mg}_2\text{SiO}_4, \text{anhydrous}}) \quad (1)$$

where  $M$  is one of the six elastic parameters  $V_0$ ,  $K_{T0}$ ,  $G_0$ ,  $K'_0$ ,  $G'_0$ . The uncertainties on  $\text{Fe}_2\text{SiO}_4$  properties at hydrous conditions were then assumed to be equal to either the anhydrous uncertainty (as published in Stixrude and Lithgow-Bertelloni (2011)) or the corresponding hydrous  $\text{Mg}_2\text{SiO}_4$  mineral uncertainty (as shown in Fig. 2), whichever was larger. To check the validity of this method, we checked if data from hydrous  $(\text{Mg}_x\text{Fe}_{1-x})_2\text{SiO}_4$  solid solution

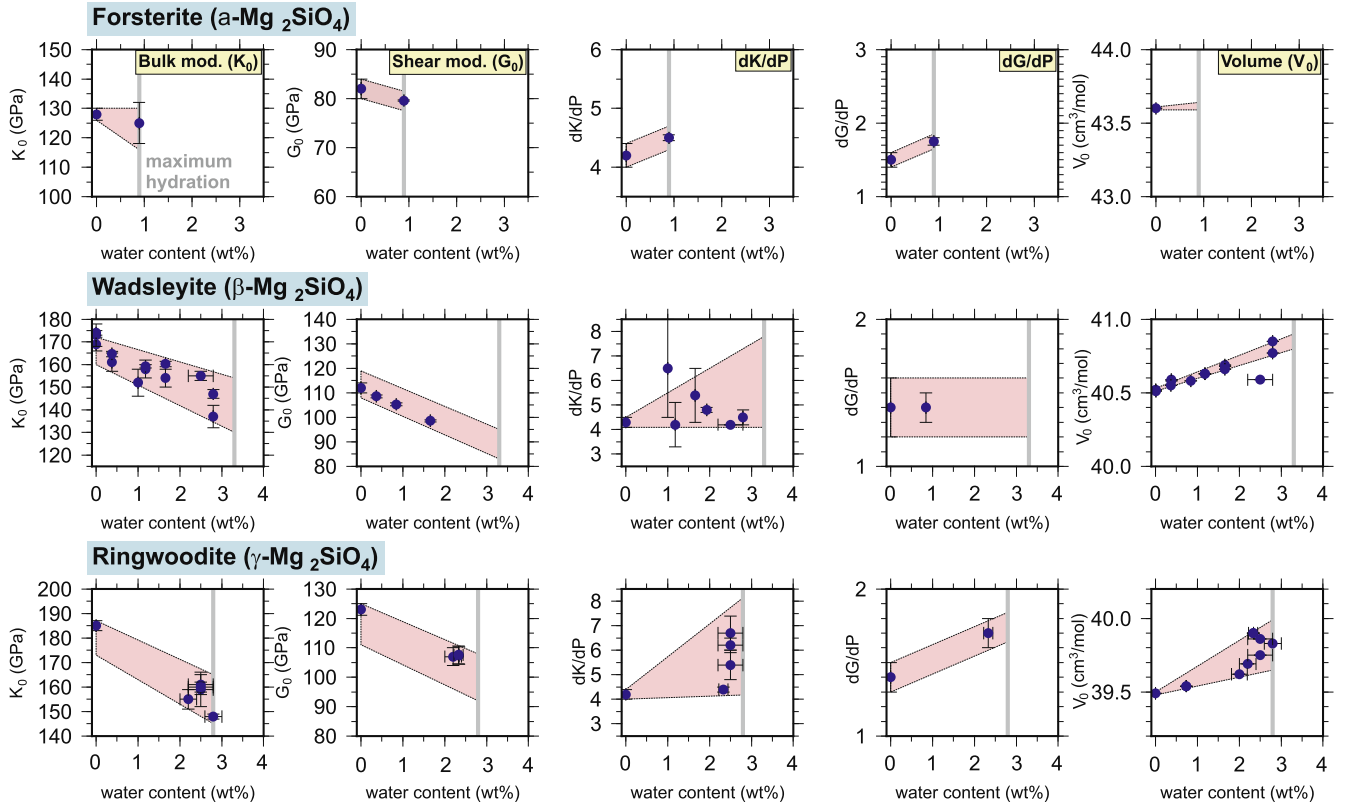


**Fig. 2.** Elastic properties of hydrous  $\text{Mg}_2\text{SiO}_4$  for olivine (forsterite), wadsleyite and ringwoodite. Blue circles correspond to experimental data with published uncertainty bars where available; grey lines indicate maximum water content per mineral. The pink areas show the uncertainty ranges we assigned to each parameter in our calculations. Numerical data values and references are listed in Tables A1–3. (For interpretation of the references to colour in this figure legend, the reader is referred to the web version of this article.)

experiments fell within the uncertainty bounds set by this method (see Fig. A1). We found that all data points did indeed fall within our assumed uncertainty bounds and conclude that they are sufficiently conservative. The resulting parameter ranges are shown in Fig. 3.

### 3.3.2. Grüneisen parameter and temperature dependence of $K$ and $G$ ( $\gamma_0$ , $q$ , $\eta_{SO}$ )

The Grüneisen parameter,  $\gamma$ , is used to set limitations on the pressure and temperature dependence of the thermal properties of a mineral, while  $q$  and  $\eta_{SO}$  represent the temperature dependence of the bulk and shear moduli respectively. These parameters may be approximated with the following formulae, after Stixrude and Lithgow-Bertelloni (2005) and Anderson (1995):

$$\gamma = \frac{\alpha K_T}{\rho C_V} \quad (2)$$

$$q_0 \approx \delta_T - K'_0 + 1 \quad \text{where } \delta_T = -(\alpha K_T)^{-1} (\partial K / \partial T)_P \quad (3)$$

$$\frac{\eta_{SO}}{\gamma} \approx \delta_G - G'_0 \quad \text{where } \delta_G \equiv -(\alpha K_T)^{-1} (\partial G / \partial T)_P \quad (4)$$

where  $C_V$  is the heat capacity at constant volume, and  $\alpha$  is the thermal expansion coefficient. While data for the temperature derivatives of the bulk and shear moduli for hydrous wadsleyite and ringwoodite have been published (Smyth and Jacobsen, 2006; Mao et al., 2012), and also for the thermal expansion coefficients of hydrous olivine, wadsleyite and ringwoodite (Smyth, 1987; Ye et al., 2009), constraints on heat capacities are lacking, and overall the available data were too sparse to allow us to characterise  $\gamma_0$ ,  $q$ , and  $\eta_{SO}$  as a function of water content. Therefore we assumed the same parameter values, and uncertainties, as those defined at

anhydrous conditions in Stixrude and Lithgow-Bertelloni (2011). Since  $\gamma_0$ ,  $q$ , and  $\eta_{SO}$  mostly fall within a small range of values for different minerals (Stixrude and Lithgow-Bertelloni, 2005), we anticipate that this assumption does not have a major influence on our results.

### 3.3.3. Helmholtz free energy and Debye temperature ( $F_0$ , $\theta_0$ )

The Helmholtz free energy  $F_0$  and Debye temperature  $\theta_0$  have a major effect on the position of the mineral phase boundaries. Though all 10 elastic parameters influence the phase boundary to some extent,  $F_0$  is the key parameter controlling the shift of the phase boundary with respect to pressure, while  $\theta_0$  determines the Clapeyron slope ( $dP/dT$ ) of the phase boundary.

Defining  $F_0$  is challenging because it is a theoretical parameter and cannot be measured directly, although it can be inferred from observations of mineral phase relations. In the database of Stixrude and Lithgow-Bertelloni (2011) it is also a relative parameter, meaning that the  $F_0$  value for each mineral has been derived relative to all the other  $F_0$ s.

$\theta_0$  can be determined from observations in several different ways, including from the mineral heat capacity (the calorimetric Debye temperature, e.g. Blackman (1955)), from vibrational entropy (Barron et al., 1957); or from the sound velocity (Anderson, 1963). Since very limited data are available for either the vibrational entropy or heat capacity of hydrous NAMs, we explored estimating Debye temperatures from the sound velocity:

$$\theta = 251 \left( \frac{\rho}{M} \right)^{1/3} \bar{v} \quad (5)$$

where  $\bar{M}$  is the mean atomic mass and  $\bar{v}$  is the Debye average sound velocity:

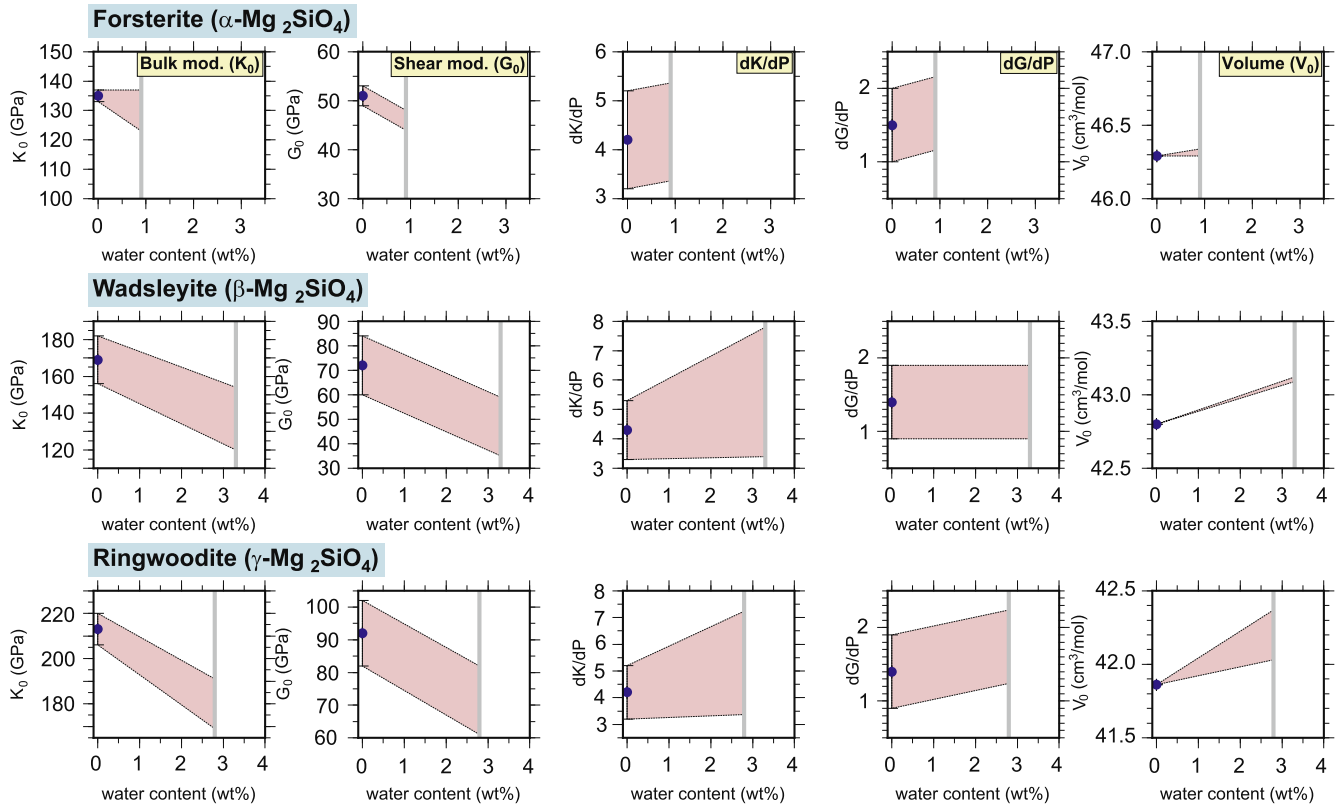


**Fig. 3.** Elastic properties of hydrous  $\text{Fe}_2\text{SiO}_4$  for olivine (fayalite), wadsleyite and ringwoodite. Grey lines indicate maximum water content per mineral and the pink area shows the uncertainty ranges we assigned to each parameter. For references see [Tables A1–3](#).

$$\bar{v} = 3^{1/3} \left( \frac{1}{V_p^3} + \frac{2}{V_s^3} \right)^{-1/3} \quad (6)$$

with  $V_p$  and  $V_s$  being the  $P$  and  $S$  wave speeds of the mineral respectively. We tested this method for several anhydrous minerals and obtained near-identical values of  $\theta_0$  to those published by [Anderson \(1995\)](#), but which differed by up to 15% from those given in [Stixrude and Lithgow-Bertelloni \(2011\)](#). We suggest that our values differ because those published by [Stixrude and Lithgow-Bertelloni \(2011\)](#) were based on vibrational entropy measurements ([Stixrude and Lithgow-Bertelloni, 2005](#)) rather than seismic velocities. Further, the global inversion procedure through which the elastic parameters were derived in [Stixrude and Lithgow-Bertelloni \(2011\)](#) likely causes  $\theta_0$  to be correlated with  $F_0$  or other parameters. Given the unavoidable correlation between  $\theta_0$  and  $F_0$ , and the discrepancy between measurements obtained by different methods, we ultimately decided to infer both  $\theta_0$  and  $F_0$  simultaneously from experimental observations of phase equilibria.

We made a compilation of experimental observations of phase equilibria in olivine, wadsleyite, ringwoodite and perovskite under hydrous conditions ([Fig. 4](#)). We used these observations to define phase boundaries between the different minerals, with conservative uncertainty ranges (blue bands, [Fig. 4](#)) which we felt represented the often limited constraints from the experimental data. Experimental observations of phase relations are typically conducted under water-saturated conditions (>3 wt% water), and it is not straightforward to obtain phase boundaries as a function of mineral water content. In our forward modelling, in which the water content of wadsleyite varies between 1 and 3.3 wt%, we have assumed the same phase boundaries and uncertainties throughout, which we believe to be reasonable given how large (c. 2 GPa, or 50 km) the uncertainties typically are. At low temperatures (up

to 1673 K), the phase boundaries are reasonably well constrained by multiple studies, especially for the pure Mg (Fo100) composition. At higher temperatures, however, data is reduced to a few data points, with observations of wadsleyite only ([Litasov et al., 2011](#)). We therefore extended the low-temperature phase boundaries to high temperatures primarily by extrapolation, assuming a constant Clapeyron slope.

To obtain values of  $\theta_0$  and  $F_0$  for the Mg end-member of each NAM, we initially assigned them randomly chosen values, while the other 8 elastic parameters ( $V_0$ ,  $K_{T0}$ ,  $G_0$ ,  $K'_0$ ,  $G'_0$ ,  $\gamma_0$ ,  $q$ ,  $\eta_{50}$ ) were selected in a Monte-Carlo procedure from within certain ranges as defined in [Section 3.3](#). The random values of  $\theta_0$  and  $F_0$  were then updated iteratively, by adjusting  $F_0$  to shift the phase boundary with respect to pressure, and  $\theta_0$  to change the Clapeyron slope, until the phase boundaries lay within the uncertainties (blue bands) shown in [Fig. 4a](#) (top left). We repeated this procedure 10,000 times to obtain a range of (correlated) values for  $\theta_0$  and  $F_0$ . A graphical representation of the correlations between our obtained values of  $\theta_0$  and  $F_0$  values is shown in [Fig. A2](#). Implicitly, these values are also correlated with the values assigned to the other 8 elastic parameters, but these correlations are weaker than between  $\theta_0$  and  $F_0$ , given that the other 8 parameters have a much smaller influence on the positions of the phase boundaries.

To our knowledge, no data are available for hydrous phase boundaries in Mg-free compositions. Limited data for mixed Mg–Fe compositions exists ([Fig. 4b](#) and [c](#)), which we used to broadly constrain the  $F_0$  and  $\theta_0$  values of the Fe end-member of each NAM: Using our own values of  $\theta_0$  and  $F_0$  for hydrous  $\text{Mg}_2\text{SiO}_4$ , and assuming that the  $\theta_0$  and  $F_0$  values for hydrous  $\text{Fe}_2\text{SiO}_4$  were the same as those published in [Stixrude and Lithgow-Bertelloni \(2011\)](#) for anhydrous  $\text{Fe}_2\text{SiO}_4$ , we checked if the phase boundaries for Mg–Fe mixtures fell within the range of experimental

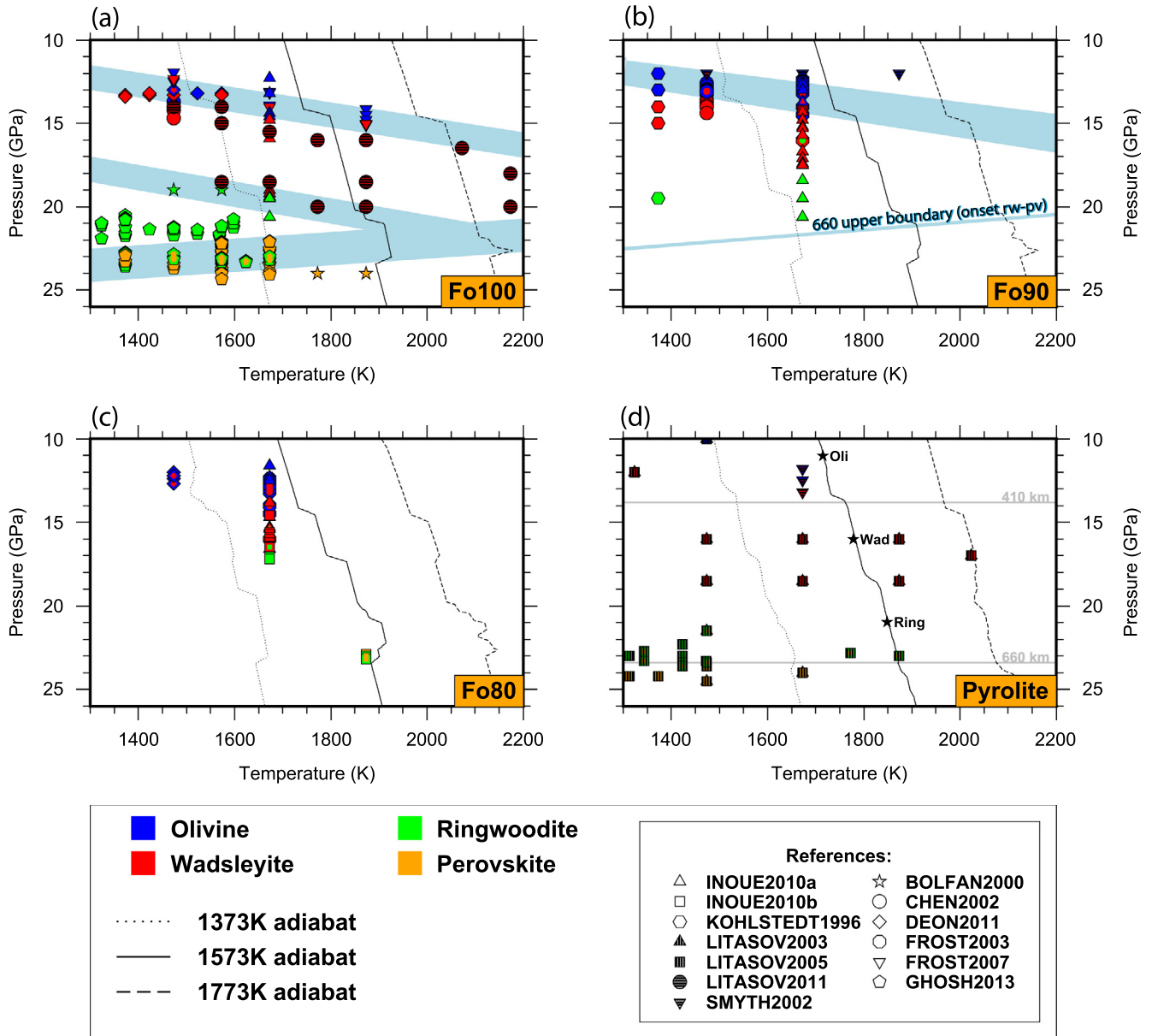


**Fig. 4.** Experimental constraints on the phase boundaries between hydrous olivine, wadsleyite, ringwoodite and perovskite for different compositions. Adiabatic  $P$ - $T$  paths under anhydrous conditions are shown for potential temperatures of 1373 K (dotted line), 1573 K (solid line) and 1773 K (dashed line). Light blue bands in the pure Mg composition (a, top left) indicate the range of possible phase boundaries that were used to derive the  $F_0$  and  $\theta_0$  values (Fig. A2) for the Mg end-member of each mineral. Light blue bands in the Fo90 composition (b, top right) indicate the allowed phase boundaries used to derive  $F_0$  and  $\theta_0$  for the Fe end-member of each mineral. Only an upper (low pressure) bound on the 660 transition (rw-pv) could be estimated, due to lack of experimental data. Data for Fo80 and pyrolitic compositions are shown for completeness but were not directly used to constrain the phase boundaries. The black stars in the pyrolitic composition (d, bottom right) indicate the median pressure and temperature of each mineral in its stability range between 300 and 800 km depth. These  $P$ - $T$  points were used to define the overall average water storage capacity for the phase (see Fig. 1). Data are taken from: Inoue et al. (2010a,b), Kohlstedt et al. (1996), Litasov and Ohtani (2003), Litasov et al. (2005, 2011), Smyth and Frost (2002), Bolfan-Casanova et al. (2000), Chen et al. (2002), Deon et al. (2011), Frost (2003), Frost and Dolejš (2007), Ghosh et al. (2013) as indicated in the symbol legend, bottom right. (For interpretation of the references to colour in this figure legend, the reader is referred to the web version of this article.)

observations for hydrous Mg-Fe mixtures (blue bands, Fig. 4b and c). This was often the case, but if not then we altered the  $F_0$  and  $\theta_0$  values for hydrous  $\text{Fe}_2\text{SiO}_4$  iteratively until they were consistent with experimental data.

While we determined  $F_0$  of the NAMs olivine, wadsleyite and ringwoodite relative to each other and to anhydrous perovskite (whose  $F_0$  is given by Stixrude and Lithgow-Bertelloni (2011)), they are not directly correlated with other minerals of the transition zone such as garnet, which are present in pyrolitic compositions (although they are indirectly connected through the  $F_0$  of perovskite). This means that we assume the phase relations in the non-olivine component are not modified by hydration of the (Mg,

$\text{Fe})_2\text{SiO}_4$ , and vice versa, which may be a simplification of the reality. Likewise, we do not include a free fluid phase or nominally hydrous silicates such as the alphabet phases (A, B, E, H...) in our modelling. These phases likely occur only in super-saturated conditions (~5–20 wt% water) and the latter also only at very low temperatures which would limit their occurrence to the coldest part of slab interiors (e.g. Frost, 1999). In this study, our focus is on constraining the potential influence of water on large-scale (100 s–1000 s km) structures that can be resolved in regional to global scale seismology, and thus on those minerals (i.e. the NAMs) which have the abundance and thermodynamic stability to host water over equivalently large length scales.

## 4. Results

We conducted a range of numerical experiments with varying water content and CFMAS composition, and summarise the key findings here. Since the water contents of olivine and ringwoodite were derived relative to wadsleyite in the ratio  $D_{\text{oli:wad:ring}} = 1:6:3$  (see Section 3.2), for the remainder of the study, the ‘water content’ of a model refers to the water content in wadsleyite. Results are shown for the following models: 0 wt%, 1.0 wt%, 2.0 wt% and 3.3 wt% water along a 1573 K adiabat (where the adiabat was computed for the anhydrous composition). For 0 wt% water we also show the results for 1373 K and 1773 K adiabats, and pyrolite + 3 mol% additional FeO (at 1573 K).

### 4.1. Discontinuity depths

In Fig. 5 we show the range (mean and standard deviation) of depths obtained for the 410 and 660 discontinuities in our models. Results are shown for both pyrolitic and Fo100, Fo90 compositions, hydrous and anhydrous. The depths of the discontinuities were determined seismically, by studying the  $V_p$  profiles of our models: At every 1 km, we computed the average velocity gradient over the previous 4 km of depth. When there was a sharp increase or decrease in the average velocity gradient (exact values for each discontinuity were determined by trial and error, but were in the range of a factor of 6–10), we defined that to be the start or end, respectively, of a discontinuity. For the 410, we searched between 350 and 500 km for a discontinuity, and for the 660, we searched between 550 and 700 km for a discontinuity. We did not attempt to identify a ‘520’ discontinuity in our models (associated with transition from wadsleyite to ringwoodite), because typically in our models the seismic changes associated with the wadsleyite to ringwoodite transition were subtle and occurring over a broad depth interval. Furthermore, in the hydrous models, the ringwoodite stability field was sometimes very small or non-existent at higher temperatures (see phase relations in Fig. 4), and there was not a clear separation of ‘520’ and ‘660’ discontinuities.

The most striking feature in Fig. 5 is the extremely large span (uncertainty) on the discontinuity depths. The Fo90 composition

has larger uncertainty for the 660 discontinuity depth than Fo100, due to limited experimental constraints for iron-bearing assemblages (e.g. see Fig. 4) – and the fact that for solid solutions (in this case Mg–Fe), phase boundaries are not univariant but involve a two-phase loop over a finite pressure interval. The effect of this uncertainty apparently reduces for pyrolitic compositions, which we believe is due to partitioning of the Fe into garnet. Furthermore, the anhydrous models display larger uncertainties than the hydrous ones. The reason for this is most likely because we allowed the elastic parameters of the anhydrous models to vary freely within the uncertainties published by Stixrude and Lithgow-Bertelloni (2011), without imposing any correlation between the parameters. Removing this correlation makes the parameters appear more poorly constrained than they actually are, and actually removes the ability to resolve an effect of temperature on the 660 discontinuity. In our hydrous models however, the  $F_0$  and  $\theta_0$  are fitted directly to experimental observations of phase equilibria (Section 3.4; Fig. 4) and are therefore intrinsically correlated. Given the large uncertainty, typically of the order of 10 s of km, it is difficult to quantify a clear distinction between hydrous and anhydrous models. The hydrous models mostly have a shallower 660 discontinuity than the anhydrous models, with a mean depth of  $\sim 630$  km, but still overlap with the anhydrous ones at the level of two standard deviations. At the 410, discontinuity depths have similar means for hydrous and anhydrous models, and cannot be distinguished within uncertainties.

### 4.2. Average velocities, densities, and velocity and density gradients

In Figs. 6–8 we compare the effect of changing water content, temperature and iron content on the average velocities, average densities, and velocity and density gradients within the transition zone, for pyrolitic composition. These averages are computed between 450 and 600 km depth, so as to avoid any influence from the 410 and 660 discontinuities.

Average  $V_p$  and  $V_s$  both decrease with increasing water content (Fig. 6). However, increases in temperature fall along almost exactly the same trend, and it is not possible to distinguish changes in temperature from changes in water from studying either  $P$  or  $S$

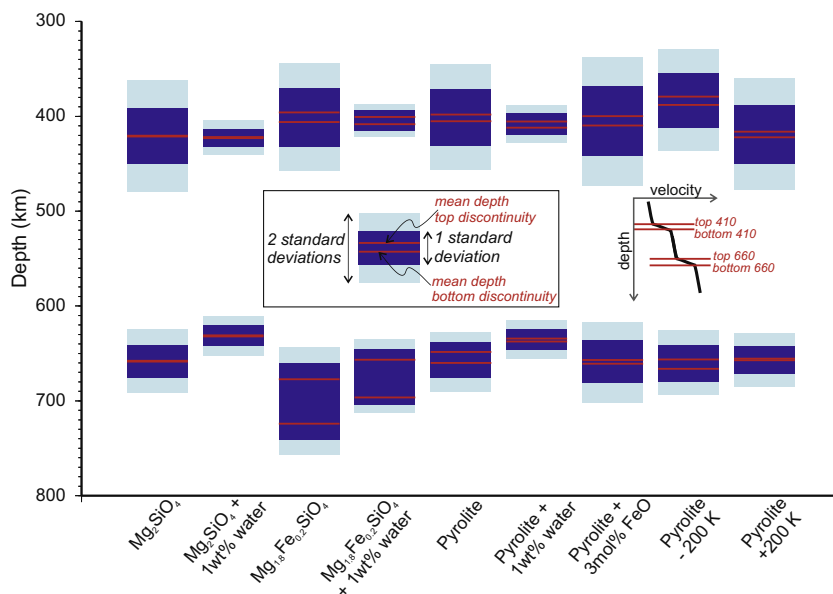


**Fig. 5.** Depths of ‘410’ and ‘660’ seismic discontinuities for hydrous and anhydrous models with various chemical compositions, along a 1573 K adiabat unless otherwise stated. Red lines show mean depths of the top and bottom of the discontinuities (since discontinuities have a finite width, see right inset); blue bands indicate the standard deviations on these depths. Bands above the upper red line indicate  $\sigma$  on the top (start depth) of the discontinuity, and below the lower red line indicate  $\sigma$  on the bottom (end depth) of the discontinuity. (For interpretation of the references to colour in this figure legend, the reader is referred to the web version of this article.)

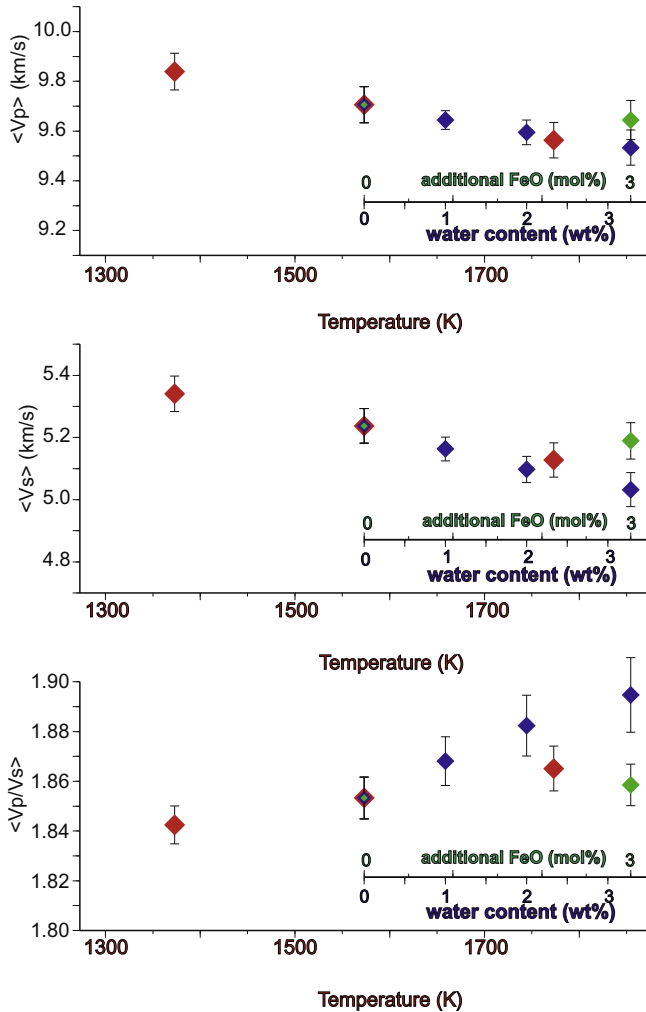


**Fig. 6.** Average  $V_p$ ,  $V_s$  and  $V_p/V_s$  between 450 and 600 km for pyrolitic composition. Vertical bars indicate 1 standard deviation. The multi-coloured (red/blue/green) diamond represents the reference case of pyrolitic composition, 0 wt% water, and temperature following an adiabat with  $T_{\text{pot}} = 1573$  K. Blue diamonds show the effect of increasing the water content (refer to blue x-axis) at constant  $T_{\text{pot}} = 1573$  K; red diamonds show the effect changing temperature (refer to red x-axis; temperatures are the adiabat potential temperature) at anhydrous conditions; green symbols show the effect of increasing the iron content (refer to green x-axis) at anhydrous conditions and constant  $T_{\text{pot}} = 1573$  K. (For interpretation of the references to colour in this figure legend, the reader is referred to the web version of this article.)

wave speeds in isolation. The average ratio  $\langle V_p/V_s \rangle$  is slightly more informative: this increases with both increasing temperature and water content, but at very high water contents (3.3 wt%) the ratio may become so high as to lie outside the range of plausible mantle temperatures ( $T_{\text{pot}} > c. 2000$  K, from extrapolation of the data points in Fig. 6, bottom panel). Increasing the iron content also decreases the average velocities and increases the ratio of  $V_p/V_s$ , and cannot be distinguished from changes in temperature.

Average  $P$  and  $S$  velocity gradients both increase with increasing water content, and decrease with increasing temperature (Fig. 7). Increasing the iron content produces very slight decrease in velocity gradient. This indicates that, when combined with information on the average velocities, average velocity gradients could be used to distinguish changes in water content from changes in temperature or iron content. However the magnitude of this effect depends also on the extent to which water is partitioned between wadsleyite and ringwoodite (see Section 5, Discussion).

Average density within the transition zone (Fig. 8) decreases for both increasing water content and temperature, but increases for

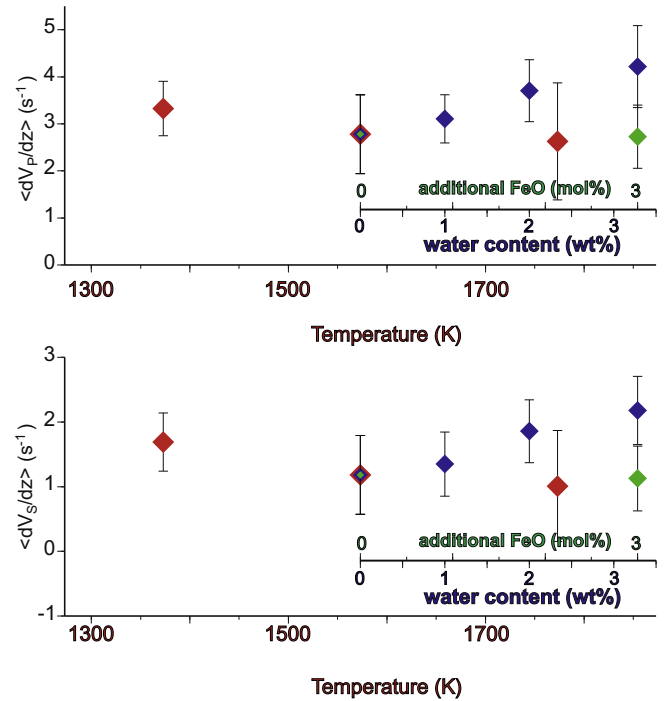


**Fig. 7.** Average  $V_p$  and  $V_s$  gradients between 450 and 600 km for hydrous and anhydrous pyrolite. Vertical bars indicate 1 standard deviation. The multi-coloured (red/blue/green) diamond represents the reference case of pyrolitic composition, 0 wt% water, and temperature following an adiabat with  $T_{\text{pot}} = 1573$  K. Blue diamonds show the effect of increasing the water content (refer to blue x-axis) at constant  $T_{\text{pot}} = 1573$  K; red diamonds show the effect changing temperature (refer to red x-axis; temperatures are the adiabat potential temperature) at anhydrous conditions; green symbols show the effect of increasing the iron content (refer to green x-axis) at anhydrous conditions and constant  $T_{\text{pot}} = 1573$  K. (For interpretation of the references to colour in this figure legend, the reader is referred to the web version of this article.)

increasing iron content. Combined with information on average velocities, this could be used to distinguish changes in iron content from other effects. Density gradients increase with increasing water content, but the effect due to temperature or iron content changes are small and difficult to characterise within the uncertainties.

#### 4.3. Impedance contrasts

Fig. 9 shows the jumps in density,  $V_p$  and  $V_s$  across the 410 and 660 discontinuities, where the ‘start’ and ‘end’ depths of the discontinuities are determined using  $V_p$ , from the maximum rate of change of  $V_p$  as a function of depth (see Section 4.1 for details). At very high water contents (3.3 wt%), 20% of the models did not display a clear 410 discontinuity, resulting from seismic similarity between olivine and wadsleyite, and were excluded from the analysis. Due to the non-Gaussian distribution of the 10,000 models (or c. 8000 in the case of 3.3 wt% water), which we believe arises from the difficulty of defining the discontinuities where they are small in amplitude or broad in depth extent, we show the full scatter of 10,000 models rather than plotting only their mean and standard deviation. At the ‘660’, identifying the discontinuity is complicated by the occurrence of a second phase transformation, garnet-to-perovskite, in addition to ringwoodite to perovskite, which can lead to double discontinuities (e.g. Shim et al., 2001). Density and velocity jumps are calculated according to  $\Delta V = 2(V_2 - V_1)/(V_2 + V_1)$  where  $V_2$  and  $V_1$  are the velocities (or densities) at the bottom and top of the discontinuities respectively.

While there is significant overlap between hydrous and anhydrous mantle models, the general trend at ‘410’ is for decreasing

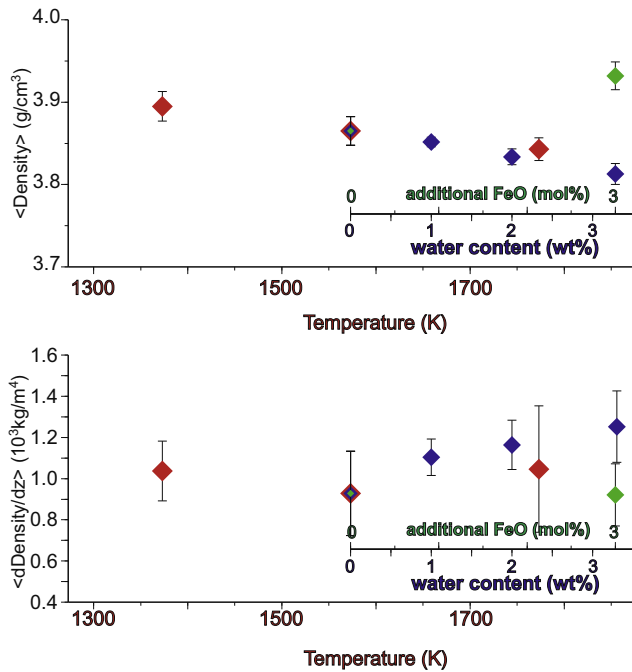


**Fig. 8.** Average density and density gradients between 450 and 600 km for hydrous and anhydrous pyrolite. Vertical bars indicate 1 standard deviation. The multi-coloured (red/blue/green) diamond represents the reference case of pyrolitic composition, 0 wt% water, and temperature following an adiabat with  $T_{\text{pot}} = 1573$  K. Blue diamonds show the effect of increasing the water content (refer to blue x-axis) at constant  $T_{\text{pot}} = 1573$  K; red diamonds show the effect changing temperature (refer to red x-axis; temperatures are the adiabat potential temperature) at anhydrous conditions; green symbols show the effect of increasing the iron content (refer to green x-axis) at anhydrous conditions and constant  $T_{\text{pot}} = 1573$  K. (For interpretation of the references to colour in this figure legend, the reader is referred to the web version of this article.)

velocity and density jumps (i.e., lower impedance contrast) with increasing water content. At ‘660’ the hydrous and anhydrous models cannot be clearly distinguished from each other, within the uncertainties.

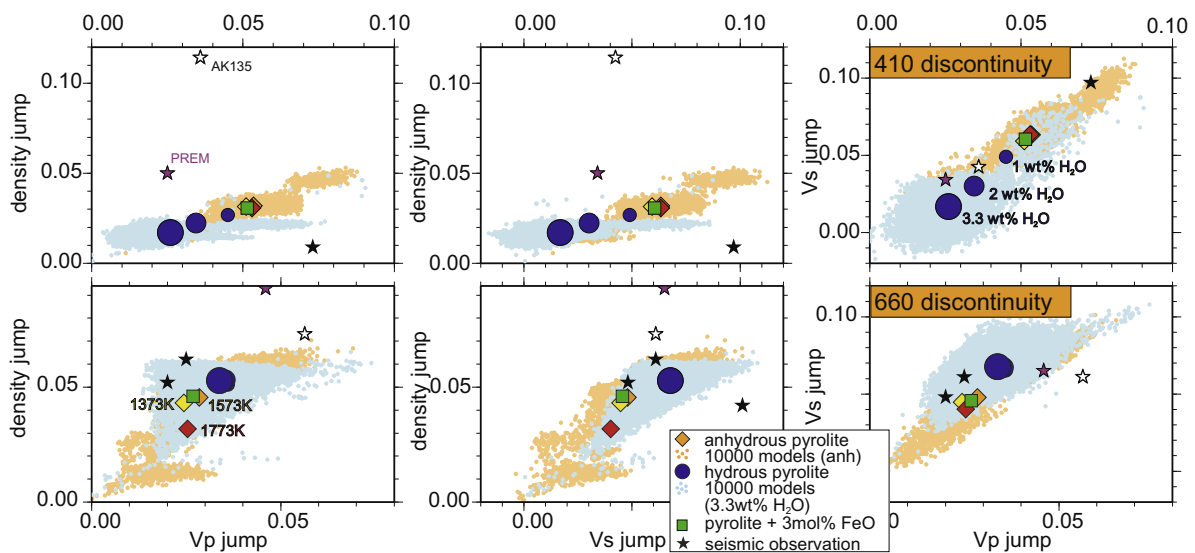


**Fig. 9.** Fractional changes in  $V_p$ ,  $V_s$  and density across the ‘410’ (top row) and ‘660’ (bottom row) discontinuities for hydrous and anhydrous pyrolite. Density and velocity jumps are calculated according to  $\Delta V = 2(V_2 - V_1)/(V_2 + V_1)$  where  $V_2$  and  $V_1$  are the velocities (or densities) at the bottom and top of the discontinuities respectively. Clouds of dots represent the range of approx. 10,000 models for 0% (light orange) and 3.3 wt% (light blue) water; circles, squares and diamonds represent the mean of 10,000 models. Seismic observations (stars) are taken from: [Dziewonski and Anderson \(1981\)](#) (i.e. PREM), [Kennett et al. \(1995\)](#) (i.e. AK135), [Shearer and Flanagan \(1999\)](#), [Estabrook and Kind \(1996\)](#), [Revenaugh and Jordan \(1991\)](#), and [Castle and Creager \(2000\)](#). (For interpretation of the references to colour in this figure legend, the reader is referred to the web version of this article.)

For comparison, we performed a literature search for observations from global and regional seismology of the impedance contrasts at 410 and 660 (Table A4, Appendix A3). Where data allowed, we extracted the jumps in density,  $V_p$  and  $V_s$  at 410 and 660 and plotted them in Fig. 9 (see references in Fig. 9). We note that the seismic observations sometimes do not overlap with our models, especially the density jumps in PREM and AK135. However we hesitate to interpret this, since we believe that overlap is likely once uncertainties and data-averaging in the seismic observations would be taken into account. PREM and AK135 in particular represent 1-D averages of the Earth’s structure and do not indicate the variability in discontinuity structure which may occur laterally.

## 5. Discussion

In Section 5.1 we evaluate the influence of the uncertainties and assumptions in our modelling on the robustness of the results presented in Section 4; in Section 5.2 we discuss the significance of those results.

### 5.1. Data uncertainties and limitations

#### 5.1.1. Mineral water contents

A key assumption in our modelling is having a constant water content per mineral, and a fixed partitioning of water between those minerals ( $D_{\text{oli:wad:ring:pv}} = 1:6:3:0$ ). The former is a restriction imposed by the thermodynamic modelling algorithm and would require extensive and non-trivial adaptation of the modelling codes, beyond the scope of this study. The latter is based on an extensive literature search (Sections 3.1 and 3.2) and is accurate within the limits of currently available data.

In reality, the storage capacities of wadsleyite and ringwoodite decrease with increasing temperature, while pressure dependence is not clear (Fig. 1). For olivine the storage capacity increases with pressure but decreases with temperature. With an adiabatic  $P$ - $T$  path through the transition zone, this may cause our models to have artificially low water content at shallower depths and artificially high water content at greater depths within the transition zone. Correcting for this effect would increase the

velocity gradients within the transition zone, and thereby enhance the seismic sensitivity to water. On the other hand, the reason that our hydrous models have elevated velocity gradients compared to anhydrous ones is in part due to water being partitioned between wadsleyite and ringwoodite in the ratio 2:1. If we assume a fixed water content of 1 wt% for both wadsleyite and ringwoodite, the average velocity gradients in the transition zone are reduced: from  $3.7(\pm 0.7) \times 10^{-3} \text{ s}^{-1}$  for  $V_p$  and  $1.9(\pm 0.5) \times 10^{-3} \text{ s}^{-1}$  for  $V_s$  (with 2 wt% water in wadsleyite, 1 wt% in ringwoodite) to  $3.1(\pm 0.6) \times 10^{-3} \text{ s}^{-1}$  for  $V_p$  and  $1.2(\pm 0.5) \times 10^{-3} \text{ s}^{-1}$  for  $V_s$  (with 1 wt% water in both minerals). However this is still elevated relative to the velocity gradients for anhydrous pyrolite at the same temperature, which are  $2.8(\pm 0.8) \times 10^{-3} \text{ s}^{-1}$  for  $V_p$  and  $1.2(\pm 0.6) \times 10^{-3} \text{ s}^{-1}$  for  $V_s$ .

Likewise, all inferences about impedance contrasts at the 410 and 660 are strongly dependent on the assumed water storage capacity of each NAM and partitioning between them. These are constrained by data from multiple studies (Section 3.1 and 3.2), and while they are the best estimate at the present time, not all experimental data agree (e.g. see Fig. 1) and we should remain open to the possibility that the data constraints, and associated seismic structures, may evolve in the future. In particular, the water content in a NAM may decrease in the presence of other minerals: Tenner et al. (2012) demonstrated that for a peridotitic bulk composition, the water storage capacity in olivine can be reduced by about 80% at 12 GPa, since the presence of garnet and orthopyroxene stabilizes hydrous melt. This effectively reduces the activity of  $\text{H}_2\text{O}$  and limits its absorption by olivine. In this scenario, the storage capacities used in our modelling represent upper bounds. Furthermore, the location and quantity of water as a function of depth within the transition zone may be controlled by geodynamic factors rather than thermodynamic requirements.

### 5.1.2. Phase boundaries

Phase boundaries have been taken conservatively to include all data points, resulting in a wide range of possible boundaries (Fig. 4). Part of this wide range arises because we compiled all observations of the NAM phase boundaries, for different water contents, into a single uncertainty range (Fig. 4). It is likely that changing the water content changes both the depth and the width (pressure interval) of the phase transformation (Frost and Dolejs, 2007), but data are insufficient to allow us to include this effect in our modelling. Additionally, with the exception of work by Litasov and co-workers (Litasov and Ohtani, 2003; Litasov et al., 2005, 2011), most experiments are performed between 1300 and 1673 K, whereas for a 1573 K adiabat we expect transition zone temperatures to lie in the range 1700–1950 K (see Fig. 4). Therefore, at higher temperatures the phase boundaries had to be inferred through extrapolation, which is inherently more uncertain than interpolation, and as such we are extremely wary of over-interpreting the discontinuity depths in hydrous transition zone models, especially the ‘660’ (Fig. 5).

### 5.1.3. Mineral elastic parameters

The largest source of uncertainty in our assumed NAM elastic parameters are the elastic properties of the Fe end-member of each mineral, which have been obtained from very limited data points (Section 3.3.1; Fig. A2). In a pyrolitic composition, Mg is volumetrically dominant over Fe (by a factor of about 8), and the seismic properties are likely most strongly influenced by the Mg end-member elastic parameters, but we should be aware of this (unavoidable) limitation in our modelling. Data for the temperature-dependence of the elastic moduli of the hydrous NAMs were also insufficient to be included in our modelling (Section 3.3.2), and we were obliged to assume the anhydrous values; we expect the potential for this assumption to distort our

results is smaller than that of the Fe end-member properties, given that the thermal parameters concerned tend not to vary greatly between different minerals (e.g. Stixrude and Lithgow-Bertelloni, 2005).

In our modelling of the seismic properties of NAMs, the parameters  $\theta_0$  and  $F_0$  have been correlated with each other from fitting phase equilibria. However the other 8 parameters  $V_0$ ,  $K_{T0}$ ,  $G_0$ ,  $K'_0$ ,  $G'_0$ ,  $\gamma_0$ ,  $q$ ,  $\eta_{S0}$  are each selected independently within their individual uncertainty ranges. In reality, correlations also exist between these parameters, especially between  $K_{T0}$  and  $K'_0$ , and hence also between their uncertainties. Our assumption of no correlation likely leads to an over-estimation of the uncertainties on the NAM seismic velocities. Experimental studies typically publish the  $K_{T0}$  value corresponding to a given  $K'_0$  value, under the assumption that the mineral compressibility follows a 3rd order Birch–Murnaghan EoS, and do not publish the correlation coefficients between  $K_{T0}$  and  $K'_0$ . Therefore with available data it was not possible for us to incorporate the inherent correlations into our modelling. The assumed uncertainty on the pressure derivatives of the hydrous NAMs is especially large (see Fig. 2 and Appendix A1), with values for hydrous ringwoodite varying between 4.0 (same as anhydrous), to up to a factor of 2 higher. We prefer however to be cautious in our approach, until more data describing the correlations between parameters become available.

## 5.2. Geophysical implications

In regional and global seismology it is relatively straightforward to map the depths of the 410 and 660 discontinuities. Observations of the discontinuities are most commonly obtained from body waves such as SS and PP precursors (e.g. Flanagan and Shearer (1998), Chambers et al. (2005b), Houser et al. (2008), Houser and Williams (2010), Day and Deuss (2013), and Lessing et al. (2014)), or P-to-S converted waves (receiver functions) (e.g. Lawrence and Shearer (2006)), but can also be inferred using surface waves (e.g. Meier et al., 2009). Both vertical and lateral resolution vary between studies and data type, but typically topography of up to 30–40 km is seen for both the ‘410’ and ‘660’ (e.g. Houser and Williams (2010), Day and Deuss (2013), and Lessing et al. (2014)), and uncertainties on the depths of the discontinuities may be as small as 8 km (Lessing et al., 2014), which at 660 km is equivalent to a pressure interval of about 0.3 GPa.

Ideally, we would like to interpret these observations quantitatively, in terms of lateral variations in temperature, mineralogy and water content, and the purpose of our study has been to investigate to what extent current mineral physics data allow this. Most existing interpretations of seismic discontinuities in terms of water content have been qualitative in nature, although a few semi-quantitative studies have been performed: Suetsugu et al. (2006) used P-wave tomography and receiver function studies, and assumed a simple linear dependence of velocities and discontinuity depth on water content, to map lateral variations in temperature and water content beneath the Japanese islands. By a similar procedure Meier et al. (2009) used surface waves to produce global maps of temperature and water content variations in the transition zone, on the basis of S-wave speed variations and discontinuity depths.

Both these, and other less quantitative, studies were based on the assumption that variations in temperature and water could be distinguished from each other through the following relation: increase in temperature produces a slower and thinner transition zone, while an increase in water content produces a slower but thicker transition zone (e.g. Smyth and Jacobsen, 2006). Our literature search revealed that while hydration of wadsleyite and ringwoodite can indeed lead to a thicker transition zone than for an

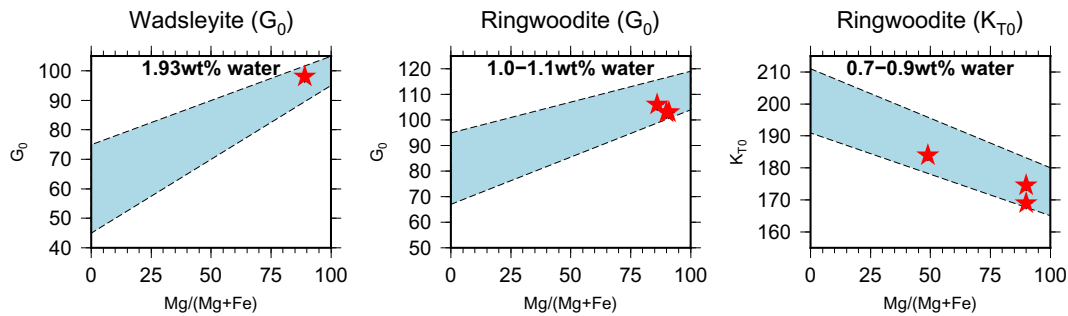


**Fig. A1.** Elastic properties of wadsleyite and ringwoodite at hydrous conditions for Mg–Fe mixtures. Left:  $G_0$  of wadsleyite, middle:  $G_0$  of ringwoodite, right:  $K_{T0}$  of ringwoodite. Red stars indicate individual measurements, blue bands represent our assigned uncertainty bounds. Exact values and associated references are shown in Tables A1–3. (For interpretation of the references to colour in this figure legend, the reader is referred to the web version of this article.)

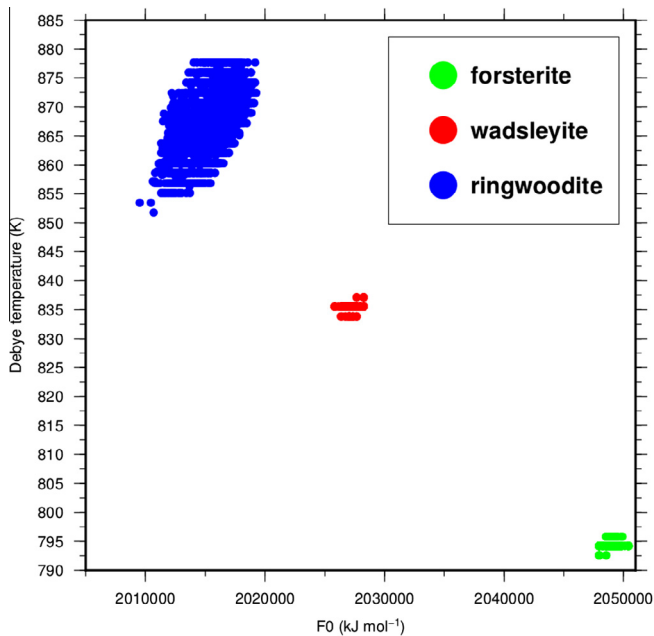


**Fig. A2.** Relation between  $F_0$  and  $\theta_0$  values derived from mineral phase equilibria (as compiled in Fig. 4).

equivalent anhydrous composition, this is only confirmed by experiments performed at around 1300–1600 K. Such temperatures may arise within cold regions of the mantle, i.e. within subducting slabs, but “normal” temperature mantle is likely several hundred degrees hotter (Fig. 4). At these higher temperatures, there are no direct experimental observations of phase transformations between hydrous minerals, and only a few observations of the existence of hydrous wadsleyite (e.g. Litasov and Ohtani, 2003; Litasov et al., 2005, 2011). We could only therefore infer the phase boundaries by extrapolation from low temperature data, and these indicated a positive Clapeyron slope for the olivine–wadsleyite transition (responsible for the ‘410’ discontinuity) and a negative Clapeyron slope for the ringwoodite–perovskite transition (responsible for the ‘660’ discontinuity). The net result of this extrapolation is a thinning of the transition zone, relative to anhydrous mantle, through a shallowing of the 660 discontinuity. In other words, within the uncertainties, it is possible that a hydrous transition zone be thinner than an anhydrous one at “normal” mantle temperature, not thicker. If our assumed extrapolation is correct, then it is not possible to distinguish thermal from water content variations on the basis of velocities plus discontinuity depths, because water and temperature have the same effect on the seismic structure and can trade off with each other. Further,

even at the colder temperatures where the phase boundaries are more tightly constrained, the variations between different experimental datasets still lead to an uncertainty on the phase boundaries of the order of 2 GPa, or 50 km. Part of this uncertainty arises from the use of different pressure calibrations in the experiments (e.g. Litasov et al. (2005), versus Ghosh et al. (2013)), which may account for up to half of the uncertainty (or 1 GPa). This uncertainty is bigger than the maximum amplitude of topography on the discontinuities (c. 30–40 km), indicating it is currently premature to use observations of discontinuity depths to map water in the mantle.

Average  $P$  and  $S$  velocities of hydrous versus anhydrous compositions at transition zone conditions are more robustly constrained (Fig. 6), but individually they trade off with changes in temperature and iron content. It is possible that combined studies of  $P$  and  $S$  waves may be more informative; in particular observations of very high  $V_P/V_S$  may be difficult to explain other than being due to water (Fig. 6). However we would be cautious of applying such interpretations at this stage, since we have modelled anharmonic velocities only. For quantitative comparison with seismic data, the models should be corrected for anelasticity, and at present few data constraints exist to accurately model the effect of water on mineral intrinsic anelasticity.

Of all the parameters we tested, average  $P$  and  $S$  velocity gradients within the transition zone appear to be most diagnostic of presence of water (Fig. 7), with higher gradients occurring in hydrous conditions, and lower gradients with increasing temperature. However, this result depends heavily on the assumption of a system in which more water is present in wadsleyite than in ringwoodite. Experimental data on both partition coefficients and water storage capacity (Sections 3.1 and 3.2) support this assumption, but we would be wary of using this metric as a direct test for water, until more experimental constraints are available, since there is still significant uncertainty in the experimental observations (Fig. 1). Additionally, velocity gradients in the transition zone are difficult to obtain from seismology – body waves are complicated by triplicated arrivals – although some constraints may be possible from surface wave studies (e.g. Cobden et al., 2008). Likewise, observations of density structure could be useful for distinguishing changes in iron content from water or temperature, but it is hard to extract density constraints from seismic observables.

In this study we have focussed on the seismic structure at the 410 and 660 discontinuities. In our models it was difficult to locate a 520 discontinuity (arising from the phase transition of wadsleyite to ringwoodite), due to a combination of data uncertainties and the seismic subtlety of the discontinuity (Section 4.1). We note however that ringwoodite becomes unstable at high temperatures, and within the uncertainties on the phase boundaries (Fig. 4), it appears that this mineral (and hence the 520 discontinuity) may

already be absent at “normal” mantle temperatures under hydrous compositions (while still present under anhydrous conditions). Tighter constraints on the hydrous phase relations would thus indicate whether the 520 (or its absence) could be used to help identify transition zone temperature or water content.

## 6. Conclusions

In summary, out of all the possible metrics that seismology can observe, it is best able to constrain lateral variations in  $P$  and  $S$  velocity, and the depths of the 410 and 660 discontinuities. Our study highlights that the expected discontinuity depths in a hydrous mantle are (currently) too poorly constrained by experimental data to allow a quantitative interpretation of the corresponding seismic observations. In particular, if the Clapeyron slope of the hydrous ring-pv phase transition is negative (possible within the uncertainties of the experimental data, see Fig. 4), then a wet transition zone may actually become thinner than a dry one at higher temperatures. This is the opposite of what happens at low temperatures and what is conventionally assumed for interpretation of seismic data (e.g. Suetsugu et al., 2006; Meier et al., 2009; Houser and Williams, 2010). Accordingly, if we would wish to use seismology to map water content in the transition zone, then the most useful data which mineral physics could provide would

be tighter constraints on the phase boundaries between hydrous minerals of the transition zone, within the resolution limits of seismology of about 0.3 GPa, and especially at  $T > 1700$  K.

## Acknowledgements

We are grateful to Steven Jacobsen and Christine Houser for providing constructive reviews which helped to improve the manuscript, and thank Jamie Connolly for advice relating to the methodology of this study. LC was funded by the Dutch Science Foundation (NWO) on Grant number NWO: VIDI 864.11.008. The research leading to these results has also received funding from the European Research Council under the European Union's Seventh Framework Programme (FP/2007–2013)/ERC Grant Agreement no. 320639.

## Appendix A1. Supplementary data for NAM elastic parameters

## Appendix A2. Density correction

At anhydrous conditions, *Perple\_X* can be used directly to calculate the density,  $V_p$  and  $V_s$  at any  $P$ ,  $T$  point within a pre-specified

**Table A1**

Elastic properties of hydrous olivine (used to assemble Figs. 3 and 4). Uncertainties given in brackets, where available.

Composition % Mg/(Mg + Fe)	wt% Water	$V_0$	$K_{T0}$	$G_0$	$dK/dP$	$dG/dP$	
100	0.9(1)						
100	0.80		125.7(2) <sup>a</sup>	79.8(1)	4.50(5) <sup>a</sup>	1.75(5)	Mao et al. (2010)
100	0.89	43.74 <sup>b</sup>					Jacobsen et al. (2008)
100	0.85	43.72 <sup>b</sup>					Smyth et al. (2005)
100	0.56	43.7 <sup>b</sup>					Smyth et al. (2005)
100	0.56	43.73 <sup>b</sup>					Smyth et al. (2005)
100	0.45	43.72 <sup>b</sup>					Smyth et al. (2005)
100	0.44	43.69 <sup>b</sup>					Smyth et al. (2005)
100	0.34	43.69 <sup>b</sup>					Smyth et al. (2005)
100	0.10	43.68 <sup>b</sup>					Smyth et al. (2005)
100	0.00	43.68 <sup>b</sup>					Smyth et al. (2005)
97	0.89		124.4(4) <sup>a</sup>	75.3(3)			Jacobsen et al. (2008)

<sup>a</sup> Values are for  $K_S$ .

<sup>b</sup> Values measured at high temperature.

**Table A2**

Elastic properties of hydrous wadsleyite (used to assemble Figs. 3 and 4). Uncertainties given in brackets, where available.

Composition % Mg/(Mg + Fe)	wt% Water	$V_0$	$K_{T0}$	$G_0$	$dK/dP$	$dG/dP$	References
100	2.5(3)	40.59	155(2)		4.3		Yusa and Inoue (1997)
100	1.00		152(6)		6.5(20)		Holl et al. (2008)
100	0.01	40.52	173(5)		4.1(15)		Holl et al. (2008)
100	0.01	40.51	174(1)		4		Holl et al. (2008)
100	0.38	40.59	161(4)		4.9(11)		Holl et al. (2008)
100	0.38	40.58	164.7(12)		4		Holl et al. (2008)
100	1.18	40.63	158(4)		4.2(9)		Holl et al. (2008)
100	1.18	40.63	159.2(8)		4		Holl et al. (2008)
100	1.66	40.69	154(4)		5.4(11)		Holl et al. (2008)
100	1.66	40.68	160.3(12)		4		Holl et al. (2008)
100	0.37	40.55	165.4(9) <sup>a</sup>	108.6(6)			Mao et al. (2008b)
100	0.84	40.58	160.3(7) <sup>a</sup>	105.3(6)			Mao et al. (2008b)
100	1.66	40.66	149.2(6) <sup>a</sup>	98.6(4)			Mao et al. (2008b)
100	0.84				4.1(1) <sup>a</sup>	1.4(1)	Mao et al. (2008a)
100	2.80	40.85	137(5)		4.5(3)		Ye et al. (2010)
100	2.80	40.77	147(2)		4		Ye et al. (2010)
89	1.93		156.2(5) <sup>a</sup>	98.0(3)	4.8(1)	1.9(1)	Mao et al. (2011)

<sup>a</sup> Values are for  $K_S$ .

range. Densities are computed per mineral by dividing the mineral molar mass  $M$  (constant) by the volume per formula unit  $V$  (variable as a function of  $P$  and  $T$ , according to the implicit equation of state). Adding water to a mineral changes its formula unit and molar mass. Due to the way in which mineral properties are implicitly calculated within *Perple\_X*, and the fact the water content varies between NAMs and between model simulations, we corrected for the change in mineral density due to water, by first computing  $V(P,T)$  with *Perple\_X*, where  $V_0$  was for the hydrous phase, and then calculating  $\rho(P,T)$  using this  $V(P,T)$ , and a modified  $M$  value.

The molar mass of a hydrous phase depends on two criteria: (1) the weight% water of the phase and (2) how the  $H^+$  atoms (or strictly speaking, protons) are incorporated within the crystal structure (i.e. type of protonation). There are three main types of protonation in NAMs: substitution of  $Mg^{2+}$  vacancies ( $Mg^{2+} \leftrightarrow 2H^+$ ); substitution of  $Si^{4+}$  vacancies ( $Si^{4+} \leftrightarrow 4H^+$ ); or a combination of these two ( $Si^{4+} \leftrightarrow 2H^+ + Mg^{2+}$ ); (Kohlstedt et al., 1996; Daniel et al., 2003; Mosenfelder et al., 2006; Litasov et al., 2007).

In the case of Mg-substitution, the resulting formula unit is  $(Mg, Fe)_{2-x_1}SiO_4H_{2x_1}$  where  $x_1$  is given by

$$x_1 = M_{anh} \left( \frac{2H^+ + O^{2-}}{W_f} + Mg^{2+} - 2H^+ \right)^{-1} \quad (A1)$$

$$\text{or } x_1 = M_{anh} \left( 22.3 + \frac{18.02}{W_f} \right)^{-1} \quad (A2)$$

where  $W_f$  is the water weight fraction,  $M_{anh}$  is the atomic mass of one formula unit at anhydrous conditions and  $H^+$ ,  $O^{2-}$  and  $Mg^{2+}$  are the atomic masses of H, O and Mg respectively. Substituting for  $x_1$  in the formula unit, using expression A2, the mass of the hydrous phase  $M_h$  is given by

$$M_h = M_{anh} \cdot (1 + 1.237W_f)^{-1} \quad (A3)$$

In a similar way to that shown above for Mg-substitution, we can compute the molar mass for Si-substitution, represented by formula unit  $(Mg, Fe)_2Si_{1-x_2}O_4H_{4x_2}$  where

$$x_2 = M_{anh} \left( 24.1 + \frac{36.0}{W_f} \right)^{-1} \quad (A4)$$

**Table A3**

Elastic properties of hydrous ringwoodite (used to assemble Figs. 3 and 4). Uncertainties given in brackets, where available.

Composition % Mg/(Mg + Fe)	wt% Water	$V_0$	$K_{T0}$	$G_0$	dK/dP	dG/dP	References
100	0.74	39.54					Smyth et al. (2003)
100	2.00(19)	39.62					Kudoh et al. (2000)
100	2.2(2)	39.69	155(4)	107(3)			Inoue et al. (1998)
100	2.33(11)	39.9	166.2(5) <sup>a</sup>	107.6(3)	4.4(1)	1.7(1)	Wang et al. (2006)
100	2.34	39.9	165.8(5) <sup>a</sup>	107.4(3)			Wang et al. (2003)
100	2.5(3)	39.86	159(7)		6.7(7)		Ye et al. (2012)
100	2.5(3)	39.75	161(4)		5.4(6)		Ye et al. (2012)
100	2.5(3)		160(2)		6.2(3)		Ye et al. (2012)
100	2.8(2)	39.83	148(1)		5		Yusa et al. (2000)
91	1	39.96	176(7) <sup>a</sup>	103(5)			Jacobsen et al. (2004)
90	0.79	39.93	174.6(27)		6.2(6)		Manghnani et al. (2005)
90	0.93	39.94	169.0(34)		7.9(9)		Smyth et al. (2004)
90	1		177(4) <sup>a</sup>	103.1(9)	5.3(4)	2.0(2)	Jacobsen and Smyth (2006)
90	0.86	39.86					Smyth et al. (2003)
89	0.79	39.86					Smyth et al. (2003)
89	0.92	39.92					Smyth et al. (2003)
87	1.07	40.08					Smyth et al. (2003)
86	1.1		175(1) <sup>a</sup>	106(1)	4.0(1)	1.6(1)	Mao et al. (2012)
49	0.7	40.9	186.5(9)		4		Ganskow et al. (2010)
61	0.37	40.58	184.1(7)		4		Ganskow et al. (2010)

<sup>a</sup> Values are for  $K_S$ .

and thus

$$M_h = M_{anh} \cdot (1 + 0.668W_f)^{-1} \quad (A5)$$

Mg-substitution is thought to be the main mechanism behind  $H^+$  storage in wadsleyite (Smyth, 1987; Jacobsen et al., 2005; Tian et al., 2012; Yang et al., 2014) and ringwoodite (51–66% according to Panero (2010), first principles study). In olivine, protonation of Mg-vacancies is thought to be the main mechanism at low pressure (Demouchy and Mackwell, 2006), but with increasing pressure Si-substitution becomes dominant (Litasov et al., 2007). According to Panero (2010), Si substitution accounts for 24–41% of  $H^+$  storage in ringwoodite.

Besides these primary mechanisms of protonation, one additional type has been found, where  $Si^{4+}$  is substituted by both  $H^+$  and  $Mg^{2+}$ . This type of substitution has been observed in ringwoodite, and may account for 8–10% of the total  $H^+$  storage (Panero, 2010). The formula unit corresponding to this type of protonation is  $(Mg, Fe)_{2+x_3}Si_{1-x_3}O_4H_{2x_3}$  where

$$x_3 = M_{anh} \left( 1.76 + \frac{18.0}{W_f} \right)^{-1} \quad (A6)$$

and thus

$$M_h = M_{anh} \cdot (1 + 0.154W_f)^{-1} \quad (A7)$$

All three types of substitution cause a decrease in the molar mass of the NAM. Combined with the effect of water on the mineral volume (see Fig. 3), which increases with increasing water content, this indicates that the mineral density decreases when water is present. Since  $H^+$  substitution in NAMs is an active area of research and we cannot currently define the percentages of each substitution mechanism in each NAM to a high precision, we made the following assumption in our calculations of the molar mass of each NAM:  $H^+$  substitution is a mixture of 50% of the first mechanism (Eq. (A3)) and 50% of the second mechanism (Eq. (A5)).

### Appendix A3. Impedance contrasts at 410 and 660, models vs observations

**Table A4**

Impedance contrasts (in%) at the 410 and 660 discontinuities, (i) from our synthetic models and (ii) from seismic observations. Impedance contrasts are given by the change in impedance  $z$  across the discontinuity, from:

$$\% \text{ change in } z = 100 \times \left[ \frac{V_2 - V_1}{(V_2 + V_1)/2} + \frac{\rho_2 - \rho_1}{(\rho_2 + \rho_1)/2} \right] \quad (\text{A8})$$

where  $z = \rho V$ . Uncertainties are shown in brackets where available (and for our models, equivalent to 1 standard deviation). Note that PREM and AK135 are not direct observations but inferred 1-D average seismic reference models. Synthetic models are for  $T_p = 1573$  K unless otherwise stated.

"410"		"660"		Model or data type	Study area	Reference
P	S	P	S			
8.5(17)	9.5(19)	7.4(17)	9.3(24)	Pyrolite, 0.0 wt% water	Synthetic	This study
8.4(14)	9.4(17)	5.7(50)	7.2(55)	Pyrolite, 0.0 wt% water, $T_p = 1773$ K	Synthetic	This study
8.2(21)	9.1(23)	7.3(17)	9.2(21)	Pyrolite, 0.0 wt% water. + 3.0 mol% FeO	Synthetic	This study
7.2(6)	7.6(11)	8.7(6)	11.6(11)	Pyrolite, 1.0 wt% water	Synthetic	This study
5.7(8)	5.2(10)	8.8(9)	12.0(14)	Pyrolite, 2.0 wt% water	Synthetic	This study
4.3(13)	3.4(16)	8.8(9)	12.0(24)	Pyrolite, 3.3 wt% water	Synthetic	This study
7.5	8.4	13.9	15.8	P and S wave travel times, normal modes	Global (PREM)	Dziewonski and Anderson (1981)
15.01	15.65	12.93	13.4	P and S wave travel times (various types)	Global (AK135)	Kennett et al. (1995)
8.2	10.6	7.2	10	PP & SS precursors	Global	Shearer and Flanagan (1999)
	4.6(10)		14.4(20)	ScS arrivals	Indo-Australia	Revenaugh and Jordan (1991)
	6.7(11)		9.9(15)	P & SH multiples, SS precursors, P-to-SV converted phases	Global	Shearer (1991)
7.6		7.2		P'P' precursors	S Atlantic, Indian Ocean, Antarctica	Xu et al. (2003)
4.6(10)	9.5(27)			PP & SS precursors	NE Asia	Chambers et al. (2005a)
6.4(15)	7.9(19)			PP & SS precursors	NW Pacific	Chambers et al. (2005a)
8.7(20)	7.7(24)			PP & SS precursors	NE Pacific	Chambers et al. (2005a)
5.1(13)	7.2(19)			PP & SS precursors	North America	Chambers et al. (2005a)
5.3(3)	7.8(6)			PP & SS precursors	Combined	Chambers et al. (2005a)
	6.7(11)		9.9(15)	SS precursors	Global	Shearer (1996)
6.5				PP precursors	Central & Northern Pacific	Rost and Weber (2002)
		8.7	12.3	PP precursors	Global	Estabrook and Kind (1996)

## References

- Anderson, D.L., 2007. *New Theory of the Earth*. Cambridge University Press.
- Anderson, O.L., 1963. A simplified method for calculating the Debye temperature from elastic constants. *J. Phys. Chem. Solids* 24, 909–917.
- Anderson, O.L., 1995. *Equations of State of Solids for Geophysics and Ceramic Science*. Oxford University Press, Oxford.
- Aubaud, C., Hirschmann, M.M., Withers, A.C., Hervig, R.L., 2008. Hydrogen partitioning between melt, clinopyroxene, and garnet at 3 GPa in a hydrous MORB with 6 wt.% H<sub>2</sub>O. *Contrib. Mineral. Petrol.* 156, 607–625.
- Barron, T., Berg, W., Morrison, J., 1957. The thermal properties of alkali halide crystals. II. Analysis of experimental results 242, 478–492.
- Bercovici, D., Karato, S., 2003. Whole-mantle convection and the transition-zone water filter. *Nature* 425, 39–44.
- Blackman, M., 1955. The specific heat of solids. In: Fluuge, S. (Ed.), *Handbuch der Physik*. Springer, pp. 325–382.
- Bolfan-Casanova, N., Keppler, H., Rubie, D., 2000. Water partitioning between nominally anhydrous minerals in the MgO–SiO<sub>2</sub>–H<sub>2</sub>O system up to 24 GPa: implications for the distribution of water in the Earth's mantle. *Earth Planet. Sci. Lett.* 182, 209–221.
- Bolfan-Casanova, N., Mackwell, S., Keppler, H., McCammon, C., Rubie, D., 2002. Pressure dependence of H solubility in magnesiowustite up to 25 GPa: implications for the storage of water in the Earth's lower mantle. *Geophys. Res. Lett.* 29, 1449.
- Bolfan-Casanova, N., Keppler, H., Rubie, D., 2003. Water partitioning at 660 km depth and evidence for very low water solubility in magnesium silicate perovskite. *Geophys. Res. Lett.* 30, 1905.
- Castle, J.C., Creager, K.C., 2000. Local sharpness and shear wave speed jump across the 660-km discontinuity. *J. Geophys. Res.-Solid Earth* 105, 6191–6200.
- Chambers, K., Deuss, A., Woodhouse, J.H., 2005a. Reflectivity of the 410-km discontinuity from PP and SS precursors. *J. Geophys. Res.-Solid Earth* 110, B02301.
- Chambers, K., Woodhouse, J.H., Deuss, A., 2005b. Topography of the 410-km discontinuity from PP and SS precursors. *Earth Planet. Sci. Lett.* 235, 610–622.
- Chen, J.H., Inoue, T., Weidner, D.J., Wu, Y.J., Vaughan, M.T., 1998. Strength and water weakening of mantle minerals, olivine, wadsleyite and ringwoodite. *Geophys. Res. Lett.* 25, 575–578.
- Chen, J.H., Inoue, T., Yurimoto, H., Weidner, D.J., 2002. Effect of water on olivine-wadsleyite phase boundary in the (Mg, Fe)<sub>2</sub>SiO<sub>4</sub> system. *Geophys. Res. Lett.* 29, 1875.
- Cobden, L., Goes, S., Cammarano, F., Connolly, J.A., 2008. Thermochemical interpretation of one-dimensional seismic reference models for the upper mantle: evidence for bias due to heterogeneity. *Geophys. J. Int.* 175, 627–648.
- Connolly, J.A.D., 1990. Multivariable phase-diagrams – an algorithm based on generalized thermodynamics. *Am. J. Sci.* 290, 666–718.
- Connolly, J.A.D., 2005. Computation of phase equilibria by linear programming: a tool for geodynamic modeling and its application to subduction zone decarbonation. *Earth Planet. Sci. Lett.* 236, 524–541.
- Daniel, I., Chamorro Perez, E., Martinez, I., Chervin, J., Dumas, P., 2003. High-pressure behavior of protonated wadsleyite: an IR spectroscopic study 1. 5685.
- Day, E.A., Deuss, A., 2013. Reconciling PP and P'P' precursor observations of a complex 660 km seismic discontinuity. *Geophys. J. Int.* 194, 834–838.
- Demouchy, S., Deloué, E., Frost, D.J., Keppler, H., 2005. Pressure and temperature-dependence of water solubility in Fe-free wadsleyite. *Am. Mineral.* 90, 1084–1091.
- Demouchy, S., Mackwell, S., 2006. Mechanisms of hydrogen incorporation and diffusion in iron-bearing olivine. *Phys. Chem. Miner.* 33, 347–355.
- Deon, F., Koch-Mueller, M., Rhede, D., Wirth, R., 2011. Water and Iron effect on the P-T-x coordinates of the 410-km discontinuity in the Earth upper mantle. *Contrib. Mineral. Petrol.* 161, 653–666.
- Dixon, J.E., Leist, L., Langmuir, C., Schilling, J.G., 2002. Recycled dehydrated lithosphere observed in plume-influenced mid-ocean-ridge basalt. *Nature* 420, 385–389.
- Drake, M.J., 2005. Origin of water in the terrestrial planets. *Meteorit. Planet. Sci.* 40, 519–527.
- Dziewonski, A.M., Anderson, D.L., 1981. Preliminary reference earth model. *Phys. Earth Planet. Inter.* 25, 297–356.
- Estabrook, C.H., Kind, R., 1996. The nature of the 660-kilometer upper-mantle seismic discontinuity from precursors to the PP phase. *Science* 274, 1179–1182.
- Ferot, A., Bolfan-Casanova, N., 2012. Water storage capacity in olivine and pyroxene to 14 GPa: implications for the water content of the Earth's upper mantle and nature of seismic discontinuities. *Earth Planet. Sci. Lett.* 349, 218–230.
- Flanagan, M.P., Shearer, P.M., 1998. Global mapping of topography on transition zone velocity discontinuities by stacking SS precursors. *J. Geophys. Res.-Solid Earth* 103, 2673–2692.
- Frost, D.J., 1999. The stability of dense hydrous magnesium silicates in Earth's transition zone and lower mantle. *Mantle Petrology: Field Observations and High Pressure Experimentation: A Tribute to Francis R. (Joe) Boyd*. The Geochemical Society (pp. 283–296).
- Frost, D.J., 2003. The structure and sharpness of (Mg, Fe)<sub>2</sub>SiO<sub>4</sub> phase transformations in the transition zone. *Earth Planet. Sci. Lett.* 216, 313–328.

- Frost, D.J., Dolejš, D., 2007. Experimental determination of the effect of H<sub>2</sub>O on the 410-km seismic discontinuity. *Earth Planet. Sci. Lett.* 256, 182–195.
- Ganskow, G., Ballaran, T.B., Langenhorst, F., 2010. Effect of iron on the compressibility of hydrous ringwoodite. *Am. Mineral.* 95, 747–753.
- Ghosh, S., Ohtani, E., Litasov, K.D., Suzuki, A., Dobson, D., Funakoshi, K., 2013. Effect of water in depleted mantle on post-spinel transition and implication for 660 km seismic discontinuity. *Earth Planet. Sci. Lett.* 371, 103–111.
- Hernández, E.R., Alfè, D., Brodholt, J., 2013. The incorporation of water into lower-mantle perovskites: a first-principles study. *Earth Planet. Sci. Lett.* 364, 37–43.
- Higo, Y., Inoue, T., Li, B., Irifune, T., Liebermann, R.C., 2006. The effect of iron on the elastic properties of ringwoodite at high pressure. *Phys. Earth Planet. Inter.* 159, 276–285.
- Hirschmann, M.M., 2006. Water, melting, and the deep Earth H<sub>2</sub>O cycle. *Annu. Rev. Earth Planet. Sci.* 34, 629–653.
- Holl, C.M., Smyth, J.R., Jacobsen, S.D., Frost, D.J., 2008. Effects of hydration on the structure and compressibility of wadsleyite, beta-(Mg<sub>2</sub>SiO<sub>4</sub>). *Am. Mineral.* 93, 598–607.
- Houser, C., Masters, G., Flanagan, M., Shearer, P., 2008. Determination and analysis of long-wavelength transition zone structure using SS precursors. *Geophys. J. Int.* 174, 178–194.
- Houser, C., Williams, Q., 2010. Reconciling Pacific 410 and 660 km discontinuity topography, transition zone shear velocity patterns, and mantle phase transitions. *Earth Planet. Sci. Lett.* 296, 255–266.
- Inoue, T., Yurimoto, H., Kudoh, Y., 1995. Hydrous modified spinel, Mg<sub>1.75</sub>SiH<sub>0.5</sub>O<sub>4</sub> – a new water reservoir in the mantle transition region. *Geophys. Res. Lett.* 22, 117–120.
- Inoue, T., Weidner, D.J., Northrup, P.A., Parise, J.B., 1998. Elastic properties of hydrous ringwoodite (gamma-phase) in Mg<sub>2</sub>SiO<sub>4</sub>. *Earth Planet. Sci. Lett.* 160, 107–113.
- Inoue, T., Ueda, T., Tanimoto, Y., Yamada, A., Irifune, T., 2010a. The effect of water on the high-pressure phase boundaries in the system Mg<sub>2</sub>SiO<sub>4</sub>–Fe<sub>2</sub>SiO<sub>4</sub>. *International Conference on High Pressure Science and Technology, Joint Aipr-22 and Hpcj-50*, 215, 012101.
- Inoue, T., Wada, T., Sasaki, R., Yurimoto, H., 2010b. Water partitioning in the Earth's mantle. *Phys. Earth Planet. Inter.* 183, 245–251.
- Jacobsen, S.D., Smyth, J.R., Spetzler, H., Holl, C.M., Frost, D.J., 2004. Sound velocities and elastic constants of iron-bearing hydrous ringwoodite. *Phys. Earth Planet. Inter.* 143, 47–56.
- Jacobsen, S.D., Demouchy, S., Frost, D.J., Ballaran, T.B., Kung, J., 2005. A systematic study of OH in hydrous wadsleyite from polarized FTIR spectroscopy and single-crystal X-ray diffraction: oxygen sites for hydrogen storage in Earth's interior. *Am. Mineral.* 90, 61–70.
- Jacobsen, S.D., Smyth, J.R., 2006. Effect of water on the sound velocities of ringwoodite in the transition zone. In: Jacobsen, S.D., van der Lee, S. (Eds.), *Earth's Deep Water Cycle*. American Geophysical Union, Washington DC, pp. 131–145.
- Jacobsen, S.D., Jiang, F., Mao, Z., Duffy, T.S., Smyth, J.R., Holl, C.M., Frost, D.J., 2008. Effects of hydration on the elastic properties of olivine. *Geophys. Res. Lett.* 35, L14303.
- Karato, S., 2011. Water distribution across the mantle transition zone and its implications for global material circulation. *Earth Planet. Sci. Lett.* 301, 413–423.
- Kawamoto, T., Hervig, R.L., Holloway, J.R., 1996. Experimental evidence for a hydrous transition zone in the early Earth's mantle. *Earth Planet. Sci. Lett.* 142, 587–592.
- Kennett, B.L.N., Engdahl, E.R., Buland, R., 1995. Constraints on seismic velocities in the Earth from travel-times. *Geophys. J. Int.* 122, 108–124.
- Kohlstedt, D.L., Keppler, H., Rubie, D.C., 1996. Solubility of water in the alpha, beta and gamma phases of (Mg, Fe)<sub>2</sub>SiO<sub>4</sub>. *Contrib. Mineral. Petrol.* 123, 345–357.
- Kudoh, Y., Kuribayashi, T., Mizobata, H., Ohtani, E., 2000. Structure and cation disorder of hydrous ringwoodite, gamma-Mg<sub>1.89</sub>Si<sub>0.98</sub>H<sub>0.30</sub>O<sub>4</sub>. *Phys. Chem. Miner.* 27, 474–479.
- Lawrence, J.F., Shearer, P.M., 2006. A global study of transition zone thickness using receiver functions. *J. Geophys. Res.-Solid Earth* 111, B06307.
- Lessing, S., Thomas, C., Rost, S., Cobden, L., Dobson, D.P., 2014. Mantle transition zone structure beneath India and Western China from migration of PP and SS precursors. *Geophys. J. Int.* 197, 396–413.
- Litasov, K., Ohtani, E., 2003. Stability of various hydrous phases in CMAS pyrolyte-H<sub>2</sub>O system up to 25 GPa. *Phys. Chem. Miner.* 30, 147–156.
- Litasov, K., Ohtani, E., 2008. Systematic study of hydrogen incorporation into Fe-bearing wadsleyite and water storage capacity of the transition zone. *Water Dyn.* 987, 113–118.
- Litasov, K.D., Ohtani, E., Sano, A., Suzuki, A., Funakoshi, K., 2005. Wet subduction versus cold subduction. *Geophys. Res. Lett.* 32, L13312.
- Litasov, K.D., Ohtani, E., Kagi, H., Jacobsen, S.D., Ghosh, S., 2007. Temperature dependence and mechanism of hydrogen incorporation in olivine at 12.5–14.0 GPa. *Geophys. Res. Lett.* 34, L16314.
- Litasov, K.D., Shatskiy, A., Ohtani, E., Katsura, T., 2011. Systematic study of hydrogen incorporation into Fe-free wadsleyite. *Phys. Chem. Miner.* 38, 75–84.
- Manghnani, M.H., Amulele, G., Smyth, J.R., Holl, C.M., Chen, G., Prakapenka, V., Frost, D.J., 2005. Equation of state of hydrous Fo<sub>90</sub> ringwoodite to 45 GPa by synchrotron powder diffraction. *Mineral. Mag.* 69, 317–323.
- Mao, Z., Jacobsen, S.D., Jiang, F., Smyth, J.R., Holl, C.M., Duffy, T.S., 2008a. Elasticity of hydrous wadsleyite to 12 GPa: implications for Earth's transition zone. *Geophys. Res. Lett.* 35, L21305.
- Mao, Z., Jacobsen, S.D., Jiang, F.M., Smyth, J.R., Holl, C.M., Frost, D.J., Duffy, T.S., 2008b. Single-crystal elasticity of wadsleyites, beta-Mg<sub>2</sub>SiO<sub>4</sub>, containing 0.37–1.66 wt.% H<sub>2</sub>O. *Earth Planet. Sci. Lett.* 268, 540–549.
- Mao, Z., Jacobsen, S.D., Jiang, F., Smyth, J.R., Holl, C.M., Frost, D.J., Duffy, T.S., 2010. Velocity crossover between hydrous and anhydrous forsterite at high pressures. *Earth Planet. Sci. Lett.* 293, 250–258.
- Mao, Z., Jacobsen, S.D., Frost, D.J., McCammon, C.A., Hauri, E.H., Duffy, T.S., 2011. Effect of hydration on the single-crystal elasticity of Fe-bearing wadsleyite to 12 GPa. *Am. Mineral.* 96, 1606–1612.
- Mao, Z., Lin, J., Jacobsen, S.D., Duffy, T.S., Chang, Y., Smyth, J.R., Frost, D.J., Hauri, E.H., Prakapenka, V.B., 2012. Sound velocities of hydrous ringwoodite to 16 GPa and 673 K. *Earth Planet. Sci. Lett.* 331, 112–119.
- Meier, U., Trampert, J., Curtis, A., 2009. Global variations of temperature and water content in the mantle transition zone from higher mode surface waves. *Earth Planet. Sci. Lett.* 282, 91–101.
- Mosenfelder, J.L., Deligne, N.I., Asimow, P.D., Rossman, G.R., 2006. Hydrogen incorporation in olivine from 2–12 GPa. *Am. Mineral.* 91, 285–294.
- Murakami, M., Hirose, K., Yurimoto, H., Nakashima, S., Takafuji, N., 2002. Water in Earth's lower mantle. *Science* 295, 1885–1887.
- Ohtani, E., Mizobata, H., Yurimoto, H., 2000. Stability of dense hydrous magnesium silicate phases in the systems Mg<sub>2</sub>SiO<sub>4</sub>–H<sub>2</sub>O and MgSiO<sub>3</sub>–H<sub>2</sub>O at pressures up to 27 GPa. *Phys. Chem. Miner.* 27, 533–544.
- Panero, W.R., 2010. First principles determination of the structure and elasticity of hydrous ringwoodite. *J. Geophys. Res.-Solid Earth* 115, B03203.
- Panero, W.R., Pigott, J.S., Reaman, D.M., Kabbes, J.E., Liu, Z., 2015. Dry (Mg, Fe)SiO<sub>3</sub> perovskite in the Earth's lower mantle. *J. Geophys. Res.: Solid Earth* 120 (2014JB011397).
- Pearson, D.G., Brenker, F.E., Nestola, F., McNeill, J., Nasdala, L., Hutchison, M.T., Matveev, S., Mather, K., Silversmit, G., Schmitz, S., Vekemans, B., Vincze, L., 2014. Hydrous mantle transition zone indicated by ringwoodite included within diamond. *Nature* 507, 221.
- Regenauer-Lieb, K., Yuen, D.A., Branlund, J., 2001. The initiation of subduction: criticality by addition of water. *Science* 294, 578–580.
- Revenaugh, J., Jordan, T.H., 1991. Mantle layering from SCS reverberations. 1. Waveform inversion of zeroth-order reverberations. *J. Geophys. Res.-Solid Earth* 96, 19749–19762.
- Richard, G., Monnerneau, M., Rabinowicz, M., 2007. Slab dehydration and fluid migration at the base of the upper mantle: implications for deep earthquake mechanisms. *Geophys. J. Int.* 168, 1291–1304.
- Rost, S., Weber, M., 2002. The upper mantle transition zone discontinuities in the Pacific as determined by short-period array data. *Earth Planet. Sci. Lett.* 204, 347–361.
- Rupke, L., Phipps Morgan, J., Dixon, J.E., 2006. Implications of subduction rehydration for Earth's deep water cycle. In: Jacobsen, S.D., van der Lee, S. (Eds.), *Earth's Deep Water Cycle*. American Geophysical Union, Washington DC, pp. 263–276.
- Schmandt, B., Jacobsen, S.D., Becker, T.W., Liu, Z., Dueker, K.G., 2014. Earth's interior. Dehydration melting at the top of the lower mantle. *Science* 344, 1265–1268.
- Shearer, P.M., 1991. Constraints on upper mantle discontinuities from observations of long-period reflected and converted phases. *J. Geophys. Res.-Solid Earth* 96, 18147–18182.
- Shearer, P.M., 1996. Transition zone velocity gradients and the 520-km discontinuity. *J. Geophys. Res.-Solid Earth* 101, 3053–3066.
- Shearer, P.M., Flanagan, M.P., 1999. Seismic velocity and density jumps across the 410- and 660-kilometer discontinuities. *Science* 285, 1545–1548.
- Shim, S., Duffy, T.S., Shen, G., 2001. The post-spinel transformation in Mg<sub>2</sub>SiO<sub>4</sub> and its relation to the 660-km seismic discontinuity. *Nature* 411, 571–574.
- Smyth, J.R., 1987. Beta-Mg<sub>2</sub>SiO<sub>4</sub> – a potential host for water in the mantle. *Am. Mineral.* 72, 1051–1055.
- Smyth, J.R., Frost, D.J., 2002. The effect of water on the 410-km discontinuity: an experimental study. *Geophys. Res. Lett.* 29, 1485.
- Smyth, J.R., Holl, C.M., Frost, D.J., Jacobsen, S.D., Langenhorst, F., McCammon, C.A., 2003. Structural systematics of hydrous ringwoodite and water in Earth's interior. *Am. Mineral.* 88, 1402–1407.
- Smyth, J.R., Holl, C.M., Frost, D.J., Jacobsen, S.D., 2004. High pressure crystal chemistry of hydrous ringwoodite and water in the Earth's interior. *Phys. Earth Planet. Inter.* 143, 271–278.
- Smyth, J.R., Frost, D.J., Nestola, F., 2005. Hydration of olivine and the Earth's deep water cycle. *Geochim. Cosmochim. Acta* 69, A746.
- Smyth, J.R., Frost, D.J., Nestola, F., Holl, C.M., Bromiley, G., 2006. Olivine hydration in the deep upper mantle: effects of temperature and silica activity. *Geophys. Res. Lett.* 33, L15301.
- Smyth, J.R., Jacobsen, S.D., 2006. Nominally anhydrous minerals and Earth's deep water cycle. In: Jacobsen, S.D., van der Lee, S. (Eds.), *Earth's Deep Water Cycle*. American Geophysical Union, Washington DC, pp. 1–11.
- Stixrude, L., Lithgow-Bertelloni, C., 2005. Thermodynamics of mantle minerals–I. Physical properties. *Geophys. J. Int.* 162, 610–632.
- Stixrude, L., Lithgow-Bertelloni, C., 2011. Thermodynamics of mantle minerals–II. Phase equilibria. *Geophys. J. Int.* 184, 1180–1213.
- Suetsugu, D., Inoue, T., Yamada, A., Zhao, D., Obayashi, M., 2006. Towards mapping the three-dimensional distribution of water in the transition zone from p-velocity tomography and 660-km discontinuity depths. *Earth's Deep Water Cycle*, 237–249.
- Sun, S.S., 1982. Chemical-composition and origin of the Earth's primitive mantle. *Geochim. Cosmochim. Acta* 46, 179–192.

- Tenner, T., Hirschmann, M., Withers, A., Ardia, P., 2012. HO storage capacity of olivine and low-Ca pyroxene from 10 to 13 GPa: consequences for dehydration melting above the transition zone. *Contrib. Miner. Petrol.* 163, 297–316.
- Tian, L., Zhao, J., Liu, W., Liu, L., Liu, H., Du, J., 2012. Effect of iron on high pressure elasticity of hydrous wadsleyite and ringwoodite by first-principles simulation. *High Pressure Res.* 32, 385–395.
- Wang, J.Y., Sinogeikin, S.V., Inoue, T., Bass, J.D., 2003. Elastic properties of hydrous ringwoodite. *Am. Mineral.* 88, 1608–1611.
- Wang, J., Sinogeikin, S.V., Inoue, T., Bass, J.D., 2006. Elastic properties of hydrous ringwoodite at high-pressure conditions. *Geophys. Res. Lett.* 33, L14308.
- Xu, F., Vidale, J.E., Earle, P.S., 2003. Survey of precursors to PP': fine structure of mantle discontinuities. *J. Geophys. Res.-Solid Earth* 108, 2024.
- Yang, X., Keppler, H., Dubrovinsky, L., Kurnosov, A., 2014. In-situ infrared spectra of hydroxyl in wadsleyite and ringwoodite at high pressure and high temperature. *Am. Mineral.* 99, 724–729.
- Ye, Y., Schwering, R.A., Smyth, J.R., 2009. Effects of hydration on thermal expansion of forsterite, wadsleyite, and ringwoodite at ambient pressure. *Am. Mineral.* 94, 899–904.
- Ye, Y., Smyth, J.R., Hushur, A., Manghnani, M.H., Lonappan, H., Dera, P., Frost, D.J., 2010. Crystal structure of hydrous wadsleyite with 2.8% H<sub>2</sub>O and compressibility to 60 GPa. *Am. Mineral.* 95, 1765–1772.
- Ye, Y., Brown, D.A., Smyth, J.R., Panero, W.R., Jacobsen, S.D., Chang, Y., Townsend, J.P., Thomas, S., Hauri, E.H., Dera, P., Frost, D.J., 2012. Compressibility and thermal expansion of hydrous ringwoodite with 2.5(3) wt% H<sub>2</sub>O. *Am. Mineral.* 97, 573–582.
- Yusa, H., Inoue, T., 1997. Compressibility of hydrous wadsleyite (beta-phase) in Mg<sub>2</sub>SiO<sub>4</sub> by high pressure X-ray diffraction. *Geophys. Res. Lett.* 24, 1831–1834.
- Yusa, H., Inoue, T., Ohishi, Y., 2000. Isothermal compressibility of hydrous ringwoodite and its relation to the mantle discontinuities. *Geophys. Res. Lett.* 27, 413–416.
- Zhao, Y.H., Ginsberg, S.B., Kohstedt, D.L., 2004. Solubility of hydrogen in olivine: dependence on temperature and iron content. *Contrib. Miner. Petrol.* 147, 155–161.